Looking for MACHOs in the spectra of fast radio bursts

Andrey Katz,[1,2] Joachim Kopp [ORCID],[1,3]★ Sergey Sibiryakov[1,4,5] and Wei Xue[1,6]

[1]*Theoretical Physics Department, CERN, CH-1211 Geneva 23, Switzerland*
[2]*Département de Physique Théorique and Center for Astroparticle Physics (CAP), Université de Genève, CH-1211 Genève 4, Switzerland*
[3]*PRISMA Cluster of Excellence and Mainz Institute for Theoretical Physics, Johannes Gutenberg University, D-55128 Mainz, Germany*
[4]*Laboratory for Particle Physics and Cosmology (LPPC), École Polytechnique Fédérale de Lausanne (EPFL), CH-1015 Lausanne, Switzerland*
[5]*Institute for Nuclear Research of the Russian Academy of Sciences, 117312 Moscow, Russia*
[6]*Department of Physics, University of Florida, Gainesville, FL 32611, USA*

ABSTRACT

We explore a novel search strategy for dark matter in the form of massive compact halo objects (MACHOs) such as primordial black holes or dense mini-haloes in the mass range from 10^{-4} M$_\odot$ to 0.1 M$_\odot$. These objects can gravitationally lens the signal of fast radio bursts (FRBs), producing a characteristic interference pattern in the frequency spectrum, similar to the previously studied femtolensing signal in gamma-ray burst spectra. Unlike traditional searches using microlensing, FRB lensing will probe the abundance of MACHOs at cosmological distance scales ($\sim$Gpc) rather than just their distribution in the neighbourhood of the Milky Way. The method is thus particularly relevant for dark mini-haloes, which may be inaccessible to microlensing due to their finite spatial extent or tidal disruption in galaxies. We find that the main complication in FRB lensing will be interstellar scintillation in the FRB's host galaxy and in the Milky Way. Scintillation is difficult to quantify because it heavily depends on turbulence in the interstellar medium, which is poorly understood. We show that, nevertheless, for realistic scintillation parameters, FRB lensing can set competitive limits on compact dark matter object, and we back our findings with explicit simulations.

Key words: gravitational lensing: micro – ISM: general – dark matter – fast radio bursts.

1 INTRODUCTION

Massive compact halo objects (MACHOs) have been widely discussed in the literature as possible dark matter candidates. In particular, a lot of attention has been paid to two classes of objects: primordial black holes (PBHs; Hawking 1971; Carr, Kuhnel & Sandstad 2016; Sasaki et al. 2018), and ultracompact mini-haloes (UCMHs; Hogan & Rees 1988; Kolb & Tkachev 1993; Kolb & Tkachev 1994; Zurek, Hogan & Quinn 2007; Hardy 2017).[1] For concreteness, we will focus our discussion on the case of PBHs, though most of our findings will apply also to other types of MACHOs.

The interesting mass range for PBHs is between 10^{-16} M$_\odot$ and 10^3 M$_\odot$ (10^{17} grams to 10^{36} grams), with M$_\odot$ being the solar mass. On the lower end of this range, the PBH abundance is strongly constrained by non-observation of the γ-ray flux that would be

produced by PBHs due to their Hawking evaporation (Carr et al. 2010; Ballesteros, Coronado-Blázquez & Gaggero 2019; Arbey, Auffinger & Silk 2020), and by measurements of the cosmic microwave background (CMB) anisotropies that would be affected by Hawking radiation in the early Universe (Poulter et al. 2019) (see also Boudaud & Cirelli 2019; DeRocco & Graham 2019; Dasgupta, Laha & Ray 2019, for constraints from injection of positrons and neutrinos). At large PBH masses, constraints are due to accretion on to PBHs, which would again affect the CMB anisotropies (Ali-Haimoud & Kamionkowski 2017). A massive effort has been put into exploring the available parameter space of PBH dark matter, in particular via microlensing searches like MACHO (Allsman et al. 2001), EROS (Tisserand et al. 2007), OGLE (Wyrzykowski et al. 2011), and most recently SUBARU-HSC (Niikura et al. 2019). Other methods to search for MACHOs in the abovementioned mass range exist, but their sensitivity is typically inferior to microlensing. Note also that several published constraints have not withstood more careful analysis and are therefore now considered invalid or controversial. Thus, big portions of MACHO parameter space remain unconstrained, while others are only loosely constrained and can still accommodate a sizable fraction of dark matter in the form of MACHOs.

★ E-mail: jkopp@cern.ch
[1]For recent *N*-body simulations of UCMHs in the context of dark matter composed of the QCD axion see Vaquero, Redondo & Stadler (2019), Buschmann, Foster & Safdi (2020), Eggemeier et al. (2019).

It is important to note that existing microlensing searches – which are responsible for essentially all the non-controversial constraints on MACHOs in the interesting mass range – are based on observations in the Milky Way or the Local Group of galaxies. Drawing conclusions on the MACHO abundance on cosmological scales thus requires extrapolation, which suffers from several uncertainties. First, translating observational results into constraints on the MACHO abundance requires assumptions about the dark matter density profile of the Milky Way, and for some observations like those by SUBARU-HSC, of the other galaxies in the Local Group. Secondly, the mass function of MACHOs and their abundance in the Local Group may differ from those on cosmological scales. Indeed, for the case of PBHs, one can expect the mass distribution to evolve in time due to accretion and mergers. Composite MACHOs such as UCMHs can be tidally disrupted inside big galactic haloes (Zhao et al. 2005; Berezinsky, Dokuchaev & Eroshenko 2006; Goerdt et al. 2007; Green & Goodwin 2007; Berezinsky, Dokuchaev & Eroshenko 2014; Tinyakov, Tkachev & Zioutas 2016; Dokuchaev, Eroshenko & Tkachev 2017; Fairbairn et al. 2018), so that more of them can be found at larger redshifts and in less dense objects than in today's Milky Way. Finally, microlensing searches cannot constrain UCMHs or other MACHOs of finite extent if their size exceeds their Einstein radius at galactic distances (Dror et al. 2019).

In this paper, we investigate a search strategy that probes MACHOs directly at cosmological distance scales. It is based on an effect which we will call *diffractive gravitational lensing*. The basic idea of diffractive lensing is that a MACHO placed between a distant source and the observer and whose mass is too small to produce two resolved images of the source still causes a phase difference between the unresolved images. This leads to characteristic interference patterns in the energy spectrum of the source. Diffractive lensing was originally proposed in the context of gamma-ray burst (GRB) sources, where it is known as femtolensing (Gould 1992; Stanek, Paczynski & Goodman 1993).[2] Diffractive lensing of GRBs could be expected to constrain MACHOs in the mass range from 10^{-17} to 10^{-14} M$_\odot$ (Barnacka, Glicenstein & Moderski 2012). However, due to the non-negligible angular sizes of typical GRBs, it turns out that the interference pattern in the spectrum would be washed out (Matsunaga & Yamamoto 2006), so that femtolensing does not currently yield bounds on the MACHO abundance (Katz et al. 2018).

We propose here to apply the diffractive lensing technique to fast radio bursts (FRBs, see e.g. reviews Katz 2018; Popov, Postnov & Pshirkov 2018; Petroff, Hessels & Lorimer 2019) rather than GRBs. As the photon wavelengths for FRBs are much longer than for GRBs, the method will be sensitive to much heavier MACHOs, namely those between 10^{-4} and 0.1 M$_\odot$. The Einstein radii of MACHOs in this mass range are much larger than those of the lenses considered in the context of GRBs, therefore the requirement on the source size is much less stringent and easily satisfied by putative FRB progenitors.

Gravitational lensing of FRBs has been considered previously in the literature: strong lensing, in particular the observation of two consecutive bursts separated in time, has been proposed in Muñoz et al. (2016) and further considered in Dai & Lu (2017), Li

et al. (2018), and Laha (2018). Such an observation would be sensitive to MACHOs of 10 M$_\odot$ to 100 M$_\odot$. Diffractive lensing of FRBs has been suggested in Zheng et al. (2014) and Eichler (2017), where it was also pointed out that the main complication in applying this technique is the distortion of FRB spectra by scintillation (Rickett 1977; Rickett 1990; Narayan 1992). The latter appears due to scattering of radio waves on the turbulent interstellar medium (ISM), leading to multipath propagation of radio signals and thus to random interference patterns in the frequency spectrum. Nevertheless, ref. Eichler (2017) argued that the lensing signal can be disentangled from scintillation by considering the temporal autocorrelation of the electromagnetic field of the radio wave.

In this paper we take further steps to explore this idea. We show that one does not need to measure the full electromagnetic field amplitude to extract the lensing signal or confirm the absence thereof. In fact, the entire analysis can be carried out in terms of the intensity (fluence) spectrum of the wave, without any need for phase information. This has practical importance as most FRB detections occur in survey mode where the full field information may not be recorded. We also demonstrate that the extraction of the lensing signal from scintillation is possible whenever these two phenomena are characterized by disparate frequency scales. Apart from the regime considered in Eichler (2017) when the two lensed images are unresolved by the scintillation screen, this also includes the case when the scintillation screen does resolve the images and distorts them incoherently, provided the lensing time delay is longer than the inverse of the decorrelation bandwidth of the scintillation. Finally, we take into account scintillation in the intergalactic medium (IGM). For realistic parameter choices we find IGM scintillation to be less relevant than scintillation in the Milky Way and in the host galaxy of the source, as long as the line-of-sight does not cross any major concentrations of ionized plasma, such as galaxy clusters. Our analytic estimates are supported by numerical simulations of FRB spectra with lensing and scintillation, using a simplified model in which the ISM and IGM are described by 1D scintillation screens.

We propose a data analysis procedure to search for the lensing signal by looking for peaks in the Fourier transform of the FRB intensity spectrum. We find that the sensitivity is improved if the smooth component of the spectrum is first divided out in order to reconstruct an approximation to the transfer function (the ratio between the emitted and recorded intensity). This procedure also reduces our sensitivity to imperfect modelling of the FRB spectrum. The search for the peaks in the Fourier transform of the transfer function is similar to the one used for resonance searches on a smooth background in collider experiments. We validate our procedure using the simulated data.

A precise modelling of scintillation is problematic due to the poor understanding of the turbulent ISM and IGM, leading to large uncertainties in the parameters governing scintillation. In spite of these complications, we will see below that there is realistic hope of extracting the lensing signal from FRB data. Moreover, the reach of the method will significantly improve in the future with an increased number of FRB detections, in particular thanks to the CHIME and SKA telescopes, which are expected to detect a few tens of FRBs per day (Macquart et al. 2015; Chawla et al. 2017). For the time being, we will explore the sensitivity as a function of the scintillation parameters and the number of FRBs.

The paper is organized as follows. In Section 2 we briefly review the formalism of gravitational diffractive lensing as well as the potential and the limitations of MACHO searches using this technique. In Section 3 we address the problem of scintillation.

---

[2]The term 'femtolensing' refers to the typical angular separation of order a femto-arcsecond between the two images produced by the lenses considered in the context of GRBs. In this paper we consider much heavier lenses corresponding to larger angular separations between images, so we prefer to designate the effect by the generic term 'diffractive lensing'.

We review the relevant properties of the ISM and IGM, and we analytically estimate the impact of scintillation on diffractive lensing of FRBs. We then proceed in Section 4 to the discussion of numerical results obtained by explicitly simulating the propagation of FRB signals. In this section, we also present our main results in the form of sensitivity estimates. We conclude in Section 5.

2 REVIEW OF DIFFRACTIVE LENSING

Consider a distant source such as an FRB, and a gravitational lens close to the line of sight. For our purposes, it is sufficient to consider the source and the lens to be point-like. In general, a point-like lens produces two images of the source, but if the lens has a small mass, the observer will not be able to resolve them. However, the photons corresponding to the two images travel different distances and experience different gravitational potentials, so their traveltimes will differ by an amount Δt. This leads to a relative phase shift $\Delta \phi = \omega \, \Delta t$, where ω is the photon energy. If $\Delta \phi \gtrsim \mathcal{O}(1)$, an interference pattern will appear in the photon energy spectrum, and may allow detection of the lens even when the two images are not resolved.

More quantitatively, the time delay between the images is given by[3]

$$\Delta t = \frac{D_L D_S}{D_{LS}} \left(\frac{|\vec{\theta} - \vec{\beta}|^2}{2} - \psi(\vec{\theta}) \right) , \tag{1}$$

where D_L, D_S, D_{LS} are the *comoving* distances between the observer and the lens, between the observer and the source, and between the lens and the source, respectively; β is the angle under which the observer would see the source in the absence of the lens, whereas θ is the angle of the lensed image; $\psi(\vec{\theta})$ stands for the lensing potential, which depends on the density profile of the lens. The lensing potential of a point-like mass M is

$$\psi(\vec{\theta}) = \theta_E^2 \log |\vec{\theta}| , \tag{2}$$

where the Einstein angle

$$\theta_E \equiv \left(4GM(1 + Z_L) \frac{D_{LS}}{D_L D_S} \right)^{1/2} \tag{3}$$

is a measure for the typical angle under which the images are observed relative to the lens. In equation (3), Z_L denotes the redshift of the lens. The positions of the images are given by the solutions to the lens equation,

$$\vec{\theta} - \vec{\beta} = \vec{\nabla} \psi(\vec{\theta}) , \tag{4}$$

which for a point-like lens gives two locations

$$\theta_{\pm} = \frac{1}{2} \left(\beta \pm \sqrt{\beta^2 + 4\theta_E^2} \right) . \tag{5}$$

Different signs of the two angles here mean that the images occur on opposite sides of the lens. Denoting $y \equiv \beta/\theta_E$, the magnifications of the two images are (Bartelmann 2010)

$$\mu_{\pm} = \frac{y^2 + 2}{2y\sqrt{y^2 + 4}} \pm \frac{1}{2} . \tag{6}$$

Their interference leads to the observed image, which, for a point-like source and lens, is magnified by a factor

$$\mu = \frac{y^2 + 2}{y\sqrt{y^2 + 4}} + \frac{2}{y\sqrt{y^2 + 4}} \sin \left(\Omega \left[\frac{y\sqrt{y^2 + 4}}{2} \right. \right.$$
$$\left. \left. + \log \left| \frac{y + \sqrt{y^2 + 4}}{y - \sqrt{y^2 + 4}} \right| \right] \right) \tag{7}$$

compared to the unlensed source. Here, the frequency dependence that creates the interference pattern enters through the dimensionless parameter

$$\Omega \equiv 4GM(1 + Z_L) \omega . \tag{8}$$

The requirement $\omega \, \Delta t \gtrsim \mathcal{O}(1)$ for the observability of lensing-induced interference patterns immediately tells us the lens masses to which a given search will be sensitive. For typical values of θ, $\beta \sim \theta_E$, the two terms in parentheses in equation (1) are of similar order, and using equation (3) for the Einstein angle, we find $\Delta t \sim R_s$, where R_s is the Schwarzschild radius of the lens. This explains why femtolensing of GRBs (Gould 1992), where photons have energies of order $10 \, \text{keV}$ to $1 \, \text{MeV}$, is most sensitive to lenses between $10^{-17} \, \text{M}_{\odot}$ and $10^{-14} \, \text{M}_{\odot}$. For fast radio bursts, with typical photon energies of order $10^{-6} \, \text{eV}$ (frequencies of order GHz), lens masses between $10^{-4} \, \text{M}_{\odot}$ and $0.1 \, \text{M}_{\odot}$ will be relevant. This mass range extends to higher masses than one might naively expect thanks to the excellent frequency resolution of radio telescopes, which allows us to resolve the interference pattern even if $\omega \, \Delta t$ is significantly larger than one.

Let us mention some caveats to the discussion above. First, we note that at $\omega \, \Delta t \sim 1$ the geometric optics approximation with two well-defined lensed images breaks down and wave optics effects need to be taken into account (Ulmer & Goodman 1995). The observed signal is then found by evaluating the full Fresnel integral over the lens plane, which leads to the observed magnification

$$\mu = \left| \frac{\Omega}{(2\pi i)\theta_E^2} \int d^2\vec{\theta} \, e^{i\omega \Delta t(\vec{\theta})} \right|^2 , \tag{9}$$

where Δt is given by equation (1). For a point source and a point-like lens, equation (9) can be evaluated analytically (Nakamura & Deguchi 1999; Katz et al. 2018), but in the general case the integral needs to be performed numerically. We compare the magnification in the geometric optics approximation to the result of a full wave optics calculation in Fig. 1. As expected, the effect of wave optics is most pronounced only at small frequencies, $\Omega \lesssim 1$. The typical frequencies at which we observe FRBs are around 1 GHz, which for lens masses $\gtrsim 10^{-4} \, \text{M}_{\odot}$ corresponds to $\Omega \gg 1$. We illustrate in Fig. 1 that in this regime wave optics corrections are negligible.

A second potential caveat is related to the angular size of the source. If the latter is too large, but unresolved by the observer, the integral over signals from different regions in the source will wash out any lensing-induced interference patterns. More precisely, this happens when the argument of the sine in equation (7) varies by an amount $\gtrsim 1$ over the angular diameter of the source. Denoting this diameter, normalized to θ_E, as σ_y, interference fringes are thus only observable if

$$\Omega \sigma_y \sqrt{y^2 + 4} \lesssim 1 . \tag{10}$$

For a $10^{-4} \, \text{M}_{\odot}$ lens about half-way between the observer and a source at 1 Gpc, and for $\Omega \sim 10$, this condition implies that wash-out is avoided for sources with a physical diameter $\lesssim 10^{13} \, \text{cm}$. This is a conservative estimate in the sense that, for heavier lenses, the maximum allowed diameter will only increase. FRBs are variable on

---

[3]We work in the units $c = \hbar = 1$ and assume that the background spacetime is described by the spatially flat Friedmann–Robertson–Walker metric.
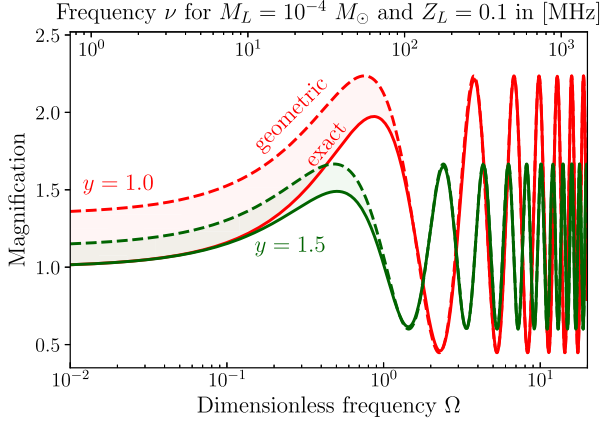
Figure 1. The diffractive lensing signal as a function of photon frequency. The vertical axis displays the ratio of the observed intensity with and without lensing, the bottom horizontal axis shows the dimensionless frequency defined in equation (8), and the top horizontal axis translates Ω into a physical frequency for a specific choice of lens mass and redshift. We compare two different angular separations between the lens and the source (red versus green lines), and we also compare the geometric optics approximation (dashed) to a full wave optics calculation (solid), concluding that, for our purposes ($\nu \sim$ GHz) geometric optics is always a valid approximation.

short time scales $t_{\rm var} \lesssim$ msec. Allowing for relativistic expansion of the emitting matter with a bulk Lorentz factor Γ, one can estimate the apparent transverse size of the source as $a_S \simeq t_{\rm var} \Gamma$ (see e.g. appendix A of ref. Katz et al. 2018 for a derivation). One concludes that for realistic values of $\Gamma < 10^5$ the size of the FRB source is irrelevant for the lensing signal.

We are going to see below that this conclusion may change in the presence of strong scintillation in the FRB host galaxy. The scintillation increases an *effective size* of the source and thereby suppresses the lensing pattern. We defer the study of this effect to the next section.

The above discussion can be generalized to the case of non-point-like lenses along the lines of ref. Katz et al. (2018). In particular, it applies to UCMHs as long as their density slope is steep enough to produce multiple images of the source.[4]

3 SCINTILLATION

We now turn to the physics of scintillation in ISM and IGM. Scintillation leads to distortions of the signals from distant FRBs that can look very similar to the distortions caused by diffractive gravitational lensing. To disentangle the two, we must therefore carefully model the physics of scintillation.

3.1 Scintillation primer

When the radio waves from a distant FRB pass through the turbulent ISM and IGM environments, they will suffer refraction and diffraction, implying that signals can reach the observer along many different trajectories. Photons travelling along different paths will interfere, leading to chaotic modulation of the observed FRB frequency spectrum. The physics here is similar to the physics of

---

[4]In the case of a power-law UCMH density profile, $\rho \propto r^{-\delta}$, multiple images appear if $\delta > 1$.

atmospheric scintillation which makes the stars flicker; as FRBs emit at different wavelength, their signals are not significantly affected by the Earth's atmosphere, but mainly by the ISM.

In the subsequent discussion, we follow refs. Narayan (1992), Lorimer & Kramer (2005), Woan (2011). Scintillation can be modelled by assuming that the turbulent plasma which is responsible for multipath propagation is confined to a thin screen. The position of the screen is chosen to be about half-way through the scintillating medium. For scintillation in the Milky Way's ISM, this typically means a scintillation screen $\mathcal{O}$(kpc) away from the observer; scintillation in the IGM can be described by a scintillation screen at a distance of $\mathcal{O}$(Gpc), for example half-way between the source and the observer. For simplicity, we perform the analysis in Minkowski spacetime, neglecting redshift effects.

Consider a plane wave of amplitude $f_{\rm in}(\omega)$ falling perpendicularly on to a scintillation screen which distorts the wavefront by adding to it a random phase $\varphi(\omega, \vec{x})$, where $\vec{x}$ is the coordinate on the screen (see Fig. 2). The signal which an observer at a point O, located at a distance $D_{\rm ScO}$ from the screen, receives is given by the Fresnel integral,

$$f_{\rm obs}(\omega) = \frac{\omega f_{\rm in}(\omega)}{2\pi i D_{\rm ScO}} \int d^2x \, e^{i\Phi(\omega, \vec{x})} \,. \qquad (11)$$

with the phase

$$\Phi(\omega, \vec{x}) = \frac{\omega x^2}{2 D_{\rm ScO}} + \varphi(\omega, \vec{x}) \,. \qquad (12)$$

Here, the first term accounts for the geometric phase, which arises because of the different distances travelled by photons passing the screen at different positions $\vec{x}$. The phase perturbation $\varphi(\omega, \vec{x})$ in the second term is characterized by the *diffractive scale* $r_{\rm diff}$, which is the distance scale on the scintillation screen over which $\varphi(\omega, \vec{x})$ varies by $\mathcal{O}(1)$. More precisely, $r_{\rm diff}$ is defined using the phase *structure function*,

$$\xi(\omega, |\Delta\vec{x}|) \equiv \left\langle \left(\varphi(\omega, \vec{x}) - \varphi(\omega, \vec{x} + \Delta\vec{x})\right)^2 \right\rangle \qquad (13)$$

through the equation

$$\xi(\omega, r_{\rm diff}) = 1 \,. \qquad (14)$$

The averaging in equation (13) is performed over an ensemble of realizations of the random phase $\varphi(\omega, \vec{x})$. Due to statistical
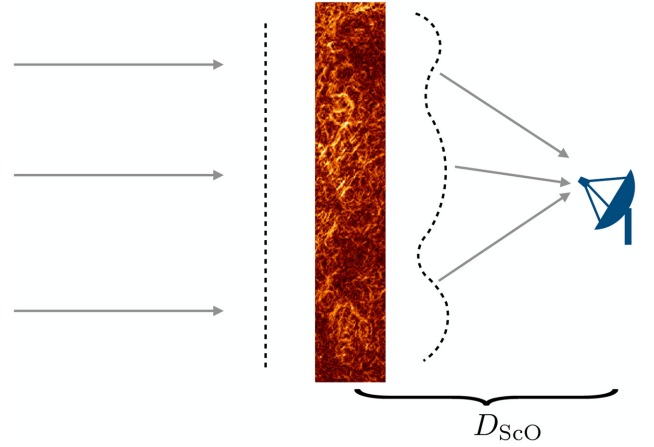

Figure 2. Distortion of a plane wave by scintillating material modelled as a thin screen. The dashed lines show the wavefront before and after the passage through the screen.

homogeneity of the scintillation screen, this is equivalent to the spatial averaging over the screen. The diffractive scale derives its name from the fact that it sets the angle $\theta_{\rm diff}$ over which radiation is typically diffracted by the screen:

$$\theta_{\rm diff} = \frac{1}{\omega\, r_{\rm diff}}\,. \tag{15}$$

As we will see below, $r_{\rm diff}$ is frequency-dependent.

In the case of weak scintillation, where the scintillation phase $\varphi(\omega, \vec{x})$ varies more slowly with $\vec{x}$ than the geometric phase, the radiation the observer receives from a given angular position on the sky comes from the first Fresnel zone of the screen, namely a region of size

$$r_F = \sqrt{D_{\rm ScO}/\omega}\,. \tag{16}$$

This is the distance over which the geometric phase changes by $\mathcal{O}(1)$, so the weak scintillation regime is characterized by the condition $r_{\rm diff} \gg r_F$. In the opposite limit of strong scintillation ($r_{\rm diff} \ll r_F$), the observed signal comes instead from a region of size

$$r_{\rm ref} = \theta_{\rm diff}\, D_{\rm ScO} = \frac{D_{\rm ScO}}{\omega\, r_{\rm diff}}\,. \tag{17}$$

$r_{\rm ref}$ is called the *refractive scale*. The different length scales on the scintillation screen are related by $r_F = \sqrt{r_{\rm diff}\, r_{\rm ref}}$.

In this paper we are only interested in the energy spectra of FRBs, not in the spatial or temporal variation of their intensity. Still, it is instructive to consider the radiation intensity as a function of position in the observer plane to understand the designation 'refractive scale' for $r_{\rm ref}$ and 'diffractive scale' for $r_{\rm diff}$ Moniez (2003). As the scintillating medium moves, the picture in the observer plane will move as well leading to temporal variations in the observed signal. In the case of strong scintillation, we expect to see a diffraction pattern of intensity variations over scales of the order of $r_{\rm diff}$ ('diffractive scintillation'), because this is by definition the scale over which $\varphi(\omega, \vec{x})$ changes by $\mathcal{O}(1)$. We also expect to see intensity variation over larger scales of the order of $r_{\rm ref}$ ('refractive scintillation'). As discussed above, each point on the screen emits radiation predominantly into a cone of the angular size $\theta_{\rm diff} = r_{\rm ref}/D_{\rm ScO}$. Depending on the gradient of the refractive index, the cones from neighbouring points will be refracted towards each other, which leads to an increase in observed radiation intensity, or away from each other, which leads to a decrease in observed radiation intensity. These intensity variations are only observable at scales larger than the cone size, that is $\gtrsim r_{\rm ref}$. They correspond to temporal variations on Time-scales $\sim r_{\rm ref}/v_\perp$, where $v_\perp$ is the transverse velocity of the scintillating medium. For the study of FRBs, refractive scintillation is not relevant as the displacement of the screen over the duration of the burst is negligible.

For weak scintillation, the observer will only register intensity variations on the scale r_F. Lines of sight separated by larger scales will effectively receive radiation from disjoint regions on the screen.

3.2 Separating lensing and scintillation

Let us now assume that the signal from a distant FRB is gravitationally lensed by a compact object such as a PBH close to the line of sight before it is distorted by a scintillation screen (see illustration in Fig. 3). For the purposes of this discussion we will restrict ourselves to lensing in the geometric optics limits. We have already seen in Section 2 that this approximation is sufficient for the lens masses we are interested in.
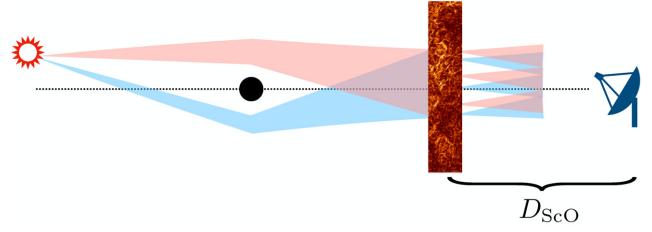
Figure 3. A fast radio burst gravitationally lensed by a compact object. The superposition of the signals corresponding to the two images passes through a scintillating medium before reaching the observer.

We describe the time-dependent FRB signal at the source as

$$F_{\rm in}(t) = \int \frac{{\rm d}\omega}{2\pi} f_{\rm in}(\omega) e^{-i\omega t}\,, \tag{18}$$

where $f_{\rm in}(\omega)$ is the amplitude of the radiation at frequency ω. Lensing in the geometric optics approximation splits this signal into two parts with different amplitudes A and B, and with a relative propagation time delay Δt (see equation 1):

$$F_{\rm lens}(t) = A F_{\rm in}(t) + B F_{\rm in}(t - \Delta t)\,. \tag{19}$$

A scintillation screen between the lens and the observer additionally imparts random noise on the lensed signal. The observed signal from a distant source, after passing a gravitational lens (e.g. a PBH) and then a scintillation screen (e.g. due to the Milky Way's ISM), can be written as

$$f_{\rm obs}(\omega) = \frac{\omega f_{\rm in}(\omega)}{2\pi i\, D_{\rm ScO}} \int d^2x\, e^{i\Phi(\omega, \vec{x})}$$
$$\left(A e^{i\omega \delta t_A(\vec{x})} + B e^{i\omega[\Delta t + \delta t_B(\vec{x})]} \right)\,. \tag{20}$$

Here, the terms $\delta t_{A,B}(\vec{x})$ account for the variation of the lensing-induced time delays with $\vec{x}$. This variation originates from the fact that the lens is seen under a different angle relative to the source from different points on the screen. Taking the square of this expression we obtain the intensity spectrum,

$$|f_{\rm obs}(\omega)|^2 = |f_{\rm in}(\omega)|^2 \Big(|\mathcal{A}(\omega)|^2 + |\mathcal{B}(\omega)|^2$$
$$+ \mathcal{A}^*(\omega)\mathcal{B}(\omega) e^{i\omega \Delta t} + \mathcal{A}(\omega)\mathcal{B}^*(\omega) e^{-i\omega \Delta t} \Big)\,, \tag{21}$$

where

$$\mathcal{A}(\omega) = \frac{A\, \omega}{2\pi i\, D_{\rm ScO}} \int d^2x\, e^{i(\Phi(\omega, \vec{x}) + \omega \delta t_A(\vec{x}))} \tag{22}$$

and similarly for $\mathcal{B}(\omega)$. We observe the presence of interference terms characteristic of diffractive lensing. If the amplitudes $\mathcal{A}$, $\mathcal{B}$ were constant, these terms would lead to regular periodic modulation of the observed intensity, as discussed in Section 2. Scintillation complicates the picture by making the amplitudes frequency dependent. Nevertheless, the lensing signal can still be extracted if the product of the amplitudes $\mathcal{A}^*(\omega)\mathcal{B}(\omega)$ contains a slowly varying component that survives upon averaging over frequency intervals $\Delta\omega \gtrsim (\Delta t)^{-1}$. Indeed, in this case the Fourier transform of the spectrum (21) will have a peak corresponding to the lensing time delay Δt.

To estimate the size of the slowly varying component we consider the product of the amplitudes smeared with a Gaussian function of width $\Delta\omega$,

$$Q(\omega, \Delta\omega) = \int \frac{{\rm d}\omega'}{\sqrt{2\pi}\,\Delta\omega} e^{-\frac{(\omega'-\omega)^2}{2\Delta\omega^2}} \mathcal{A}^*(\omega')\mathcal{B}(\omega')\,. \tag{23}$$

Its characteristic value is given by the ensemble average $\langle |Q(\omega, \Delta\omega)|^2 \rangle$ over random realizations of the scintillation phase. This average involves the correlator of four amplitudes,

$$\langle \mathcal{A}^*(\omega')\mathcal{B}(\omega')\mathcal{A}(\omega'')\mathcal{B}^*(\omega'') \rangle . \tag{24}$$

In the case of strong scintillation the integral (22) extends over many Fresnel regions. The contributions of different regions are essentially statistically independent. Then, by the central limiting theorem, the statistics of the amplitudes $\mathcal{A}(\omega)$ and $\mathcal{B}(\omega)$ are close to Gaussian and we can replace (24) by

$$\langle \mathcal{A}^*(\omega')\mathcal{A}(\omega'') \rangle \langle \mathcal{B}(\omega')\mathcal{B}^*(\omega'') \rangle + \langle \mathcal{A}^*(\omega')\mathcal{B}(\omega') \rangle \langle \mathcal{A}(\omega'')\mathcal{B}^*(\omega'') \rangle , \tag{25}$$

where we have used that the correlator $\langle \mathcal{A}(\omega')\mathcal{B}(\omega'') \rangle$ vanishes. Our next task is to estimate the two-point correlators entering into this expression.

Let us start with

$$\langle \mathcal{A}^*(\omega')\mathcal{A}(\omega'') \rangle \equiv A^2 \mathcal{C}_0(\omega'' - \omega') , \tag{26}$$

where on the r.h.s. we introduced the frequency autocorrelation function for the signal coming from a single image. A similar equation holds for the correlator of the $\mathcal{B}$ amplitudes. An important characteristic of the scintillation-induced noise is its decorrelation bandwidth ω_{dec}. The noise amplitude is correlated at frequencies separated by less than ω_{dec} and uncorrelated otherwise. An estimate for ω_{dec} is obtained by recalling that the observer sees a patch of diameter r_{ref} on the scintillation screen. Over this distance, the geometric phase (first term in equation 12) varies by an amount $\omega r_{\text{ref}}^2/(2D_{\text{ScO}})$. A shift in frequency by $2D_{\text{ScO}}/r_{\text{ref}}^2$ changes the phases at different points of the patch by order unity resulting in decorrelation of the scintillation noise. Thus we arrive at the estimate

$$\omega_{\text{dec}} \sim \frac{2D_{\text{ScO}}}{r_{\text{ref}}^2} . \tag{27}$$

Note that we assumed above that the random phase $\varphi(\omega, \vec{x})$ (second term in equation 12) changes with frequency in the same way or more slowly than the geometric phase. This is indeed the case for scintillation in ionized plasma, where φ is inversely proportional to frequency (see the next subsection). The decorrelation bandwidth sets the range of the autocorrelation function (26): one expects that $\mathcal{C}_0$ is of the order of 1 if $|\omega'' - \omega'| \lesssim \omega_{\text{dec}}$ and quickly decreases outside this range.

The second term in equation (25) contains the cross-correlation between the amplitudes of the two lensed images at fixed frequency $\langle \mathcal{A}^*(\omega)\mathcal{B}(\omega) \rangle$. Its magnitude depends on whether the two images are distorted by scintillation screen in the same way (coherently) or independently (incoherently). In the first case the correlation is order-one, whereas in the second case it is suppressed. To determine the conditions for coherent/incoherent distortion, let us consider the variation $\delta t_B(\vec{x}) - \delta t_A(\vec{x})$ of the lensing-induced time delay over the scintillation screen. This can be found by noting that a change of position on the screen changes the difference between the viewing angles of the lens and the source by $\delta\beta = (xD_{LS})/(D_L D_S)$. Hence, the variation of the time delay is given by

$$\delta t_B - \delta t_A = \frac{d\Delta t}{d\vec{\beta}} \cdot \frac{\vec{x} D_{LS}}{D_L D_S} = \Delta\vec{\theta} \, \vec{x} , \tag{28}$$

where $\Delta\vec{\theta}$ is the angular distance between the *A* and *B* images. In the second equality we have used equation (1). Due to scintillation, the observer receives photons from a region of size r_{ref} on the screen. If

the variation of the lensing-induced phase over this region is small, we can neglect it in the integral (22) for the amplitudes and obtain,

$$\langle \mathcal{A}^*(\omega)\mathcal{B}(\omega) \rangle = AB \left\langle \left| \frac{\omega}{2\pi i D_{\text{ScO}}} \int d^2x \, e^{i\Phi(\omega,\vec{x})} \right|^2 \right\rangle \sim AB . \tag{29}$$

In the opposite regime a fast lensing-phase variation leads to strong suppression of the correlation between the amplitudes. Thus, in general we can write,

$$\langle \mathcal{A}^*(\omega)\mathcal{B}(\omega) \rangle = AB \cdot \mathcal{U}(\omega \, \Delta\theta \, r_{\text{ref}}) , \tag{30}$$

where the function $\mathcal{U}$ is of the order of unity when its argument is less than 1 and quickly vanishes outside this range.[5]

We now return to the smeared amplitude of the interference term (equation 23). Collecting our previous results from equations (26) and (30) we obtain,

$$\langle |Q(\omega, \Delta\omega)|^2 \rangle = A^2 B^2 \left\{ \int \frac{d\omega_-}{2\sqrt{\pi} \Delta\omega} e^{-\frac{\omega_-^2}{4\Delta\omega^2}} \left| \mathcal{C}_0(\omega_-) \right|^2 \right.$$
$$\left. + \left| \bar{\mathcal{U}}(\omega \, \Delta\theta \, r_{\text{ref}}) \right|^2 \right\} , \tag{31}$$

where we have denoted by $\bar{\mathcal{U}}$ the correlator (30) averaged over a range of frequencies $\Delta\omega$. Extraction of the lensing signal is possible whenever either of the two terms in brackets is sizable, implying that the interference amplitude has a piece that does not vanish when averaged over frequency intervals $\Delta\omega \gtrsim (\Delta t)^{-1}$. If $\Delta\omega$ is smaller than the decorrelation bandwidth, the autocorrelation function in the first term can be replaced by unity and the whole integral equals 1. In the opposite regime $\Delta\omega \gg \omega_{\text{dec}}$ it becomes suppressed as $\omega_{\text{dec}}/\Delta\omega$. Recalling that we want the averaging interval $\Delta\omega$ to be at least as large as $(\Delta t)^{-1}$, we conclude that the first term in equation (31) is $\mathcal{O}(1)$ for long lensing delays $\Delta t \gg (\omega_{\text{dec}})^{-1}$. The magnitude of the second term in equation (31) is controlled by the angular separation between the lensed images. Given that the characteristic size of $\Delta\theta$ is set by the Einstein angle θ_E, we can rephrase the condition for this term to be significant as $\omega \, \theta_E \, r_{\text{ref}} < 1$. In this way we arrive at four possible scenarios, which are illustrated in Fig. 4:

(a) $\Delta t \gg (\omega_{\text{dec}})^{-1}$, $\omega \, \theta_E \, r_{\text{ref}} \ll 1$ (region above the red and blue lines in Fig. 4). In this case, both terms in equation (31) are sizeable. The lensing phase $\omega\Delta t$ varies much faster with frequency than the scintillation phase $\Phi(\omega, \vec{x})$, and does not change substantially across the scintillation screen. Therefore, a clear lensing pattern can be observed in the form of rapid periodic variations of the radiation intensity with ω. The envelope of the lensing wiggles in the frequency spectrum is modulated over frequency intervals $\gg (\Delta t)^{-1}$ by scintillation effects and by the variation of the lensing phase across the screen.

This behaviour is clearly visible in the top panels of Fig. 5. In the left-hand part of this figure, we show the transfer function

$$|T(\nu)|^2 \equiv \left| \frac{f_{\text{obs}}(\nu)}{f_{\text{in}}(\nu)} \right|^2 , \tag{32}$$

while in the middle part, we plot the autocorrelation function of the normalized signal amplitude,

$$\mathcal{C}(d\nu) \equiv \frac{\left| \langle T^*(\nu) \, T(\nu + d\nu) \rangle \right|}{\langle |T(\nu)|^2 \rangle} . \tag{33}$$

---

[5]Under general assumptions about the statistical properties of the scintillation phase, one can show that $\mathcal{U}(z)$ is exponentially suppressed at $z > 1$.
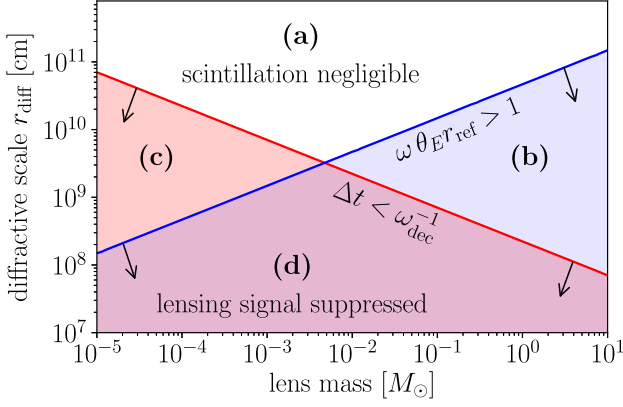
Figure 4. Observability of FRB lensing by compact dark matter objects as a function of the lens mass M and of the diffractive scale corresponding to interstellar scintillation in the Milky Way. We assume an FRB at a comoving distance of 1 Gpc, and a lens at 0.5 Gpc. The angular separation between the lens and the (unlensed) source, normalized to the Einstein angle, is $y = \beta/\theta_E = 0.5$. We consider 1 GHz radio waves, which are perturbed by a scintillation screen at 1 kpc from the observer.

Here $\nu = \omega/(2\pi)$ is the radiation frequency and averaging is performed over a large frequency interval. In the right-hand part of Fig. 5, we show the Fourier transform of $|T(\nu)|^2$. As expected, the lensing signal is clearly visible, with its envelope only marginally modulated due to scintillation.

(b) $\Delta t \gg (\omega_{\text{dec}})^{-1}$, $\omega \theta_E r_{\text{ref}} \gg 1$ (region below the blue, but above the red line in Fig. 4). The variation of the lensing phase over the scintillation screen is fast, so the two lensed images are distorted incoherently. Thus, the second term in equation (31) is suppressed. Nevertheless, the first term remains of the order of unity as the amplitudes $\mathcal{A}(\omega)$ and $\mathcal{B}(\omega)$ vary slowly as functions of ω. A clear lensing signal still survives both in the transfer function and in the autocorrelation function. This is illustrated in the second row of panels in Fig. 5.

(c) $\Delta t \ll (\omega_{\text{dec}})^{-1}$, $\omega \theta_E r_{\text{ref}} \ll 1$ (region below the red, but above the blue line in Fig. 4). When the time delay Δt between the two lensed images is shorter than the inverse of the decorrelation bandwidth ω_{dec}, the scintillation factor $e^{i\Phi(\omega,\vec{x})}$ in equation (20) varies much faster than the lensing factor $e^{i\omega\Delta t}$. The first term in equation (31) is then small. On the other hand, we can neglect the variation of the lensing phase over the screen, $\omega \, \delta t(\vec{x})$, so the two lensed images are distorted coherently and the second term in equation (23) is sizable. The lensing signal will be discernible as a modulation of the envelope of an otherwise chaotic spectrum. Indeed, the panels in the third row in Fig. 5 illustrate this behaviour: we observe high-frequency scintillation noise, superimposed on regular periodic oscillations due to lensing. As expected, the signal disappears from the autocorrelation function, but remains in the Fourier transform of the transfer function.

(d) $\Delta t \ll (\omega_{\text{dec}})^{-1}$, $\omega \theta_E r_{\text{ref}} \gg 1$ (region below the red and blue lines in Fig. 4). In this case, the fast variations of the scintillation factor $e^{i\Phi(\omega,\vec{x})}$ combines with incoherent distortion of the images. The amplitude $\mathcal{A}^*(\omega)\mathcal{B}(\omega)$ of the interference term in equation (21) does not contain a slowly varying component and the lensing signal is strongly suppressed, see the last row in Fig. 5.

We conclude that a lensing signal is in principle observable in regimes (a), (b), and (c), but strongly suppressed or completely unobservable in regime (d).

However, there are practical considerations that may render the signal unobservable even in regimes (a), (b), and (c). The distance between subsequent lensing fringes in the spectrum, $(\Delta t)^{-1}$, should be significantly larger than the instrumental frequency resolution, but significantly smaller than the instrumental bandwidth. The first condition is violated for too large lens masses, the second one for lens masses that are too small.[6] This effectively restricts the search for compact objects using diffractive lensing of FRBs to the mass range between $\sim 10^{-4} \, \text{M}_\odot$ and $\sim 0.1 \, \text{M}_\odot$.

The above discussion applies also to the case of a scintillation screen placed between the source and the lens (see Fig. 6). This setup describes scintillation in the ISM of the FRB host galaxy or in the IGM between the lens and the host. The amplitude of the observed signal is again given by equation (20), with the screen–observer distance D_{ScO} replaced by the screen–source distance D_{ScS}. The rest of the analysis proceeds without change. Notice that strong scintillation effectively spreads the source into a patch of radius r_{ref} on the scintillation screen. The condition $\omega \theta_E r_{\text{ref}} < 1$ for coherent distortion of the lensed images can then be reinterpreted as the restriction (10) on the size of the source required for diffractive lensing. One may wonder why one can discern the lensing pattern in regime (b) even if this condition is violated. The reason is that the signal from each point on the lensing screen is correlated at different frequencies within a finite decorrelation bandwidth, which is not the case for a truly incoherent source.

3.3 The turbulent interstellar and intergalatic medium

For a quantitative description of scintillation and its effect on FRB signals, we need to discuss in more detail the properties of the ISM and IGM. We focus in particular on interstellar and intergalactic plasma, neglecting the neutral gas. The reason is that the refractive index of a plasma deviates from unity by much more than the refractive index of neutral gas, so that its impact on the phase fluctuations that cause scintillation is much larger.

3.3.1 The interstellar medium

Propagation in plasma modifies the dispersion relation of electromagnetic waves with wavenumber k,

$$\omega^2 = k^2 + \omega_p^2 \,. \tag{34}$$

Here the plasma frequency is expressed in terms of the electron number density n_e, the electron mass m_e, and the electromagnetic fine structure constant α,

$$\omega_p = \sqrt{\frac{4\pi \alpha n_e}{m_e}} \,. \tag{35}$$

As a consequence, a wave propagating in plasma acquires a frequency-dependent phase shift,

$$\varphi(\vec{x}) = -\frac{2\pi \alpha}{m_e \omega} \int n_e(\vec{x}, z) \, \mathrm{d}z \,, \tag{36}$$

[6]Note that at masses $\gtrsim 10 \, \text{M}_\odot$ one would expect lensing time delays $\gtrsim 10^{-3}$ s, comparable to the typical duration of FRBs. This would correspond to modulation on kHz scales in the frequency spectrum. However, in this regime, it seems more convenient to work directly with the temporal profile of the FRBs (Dai & Lu 2017).
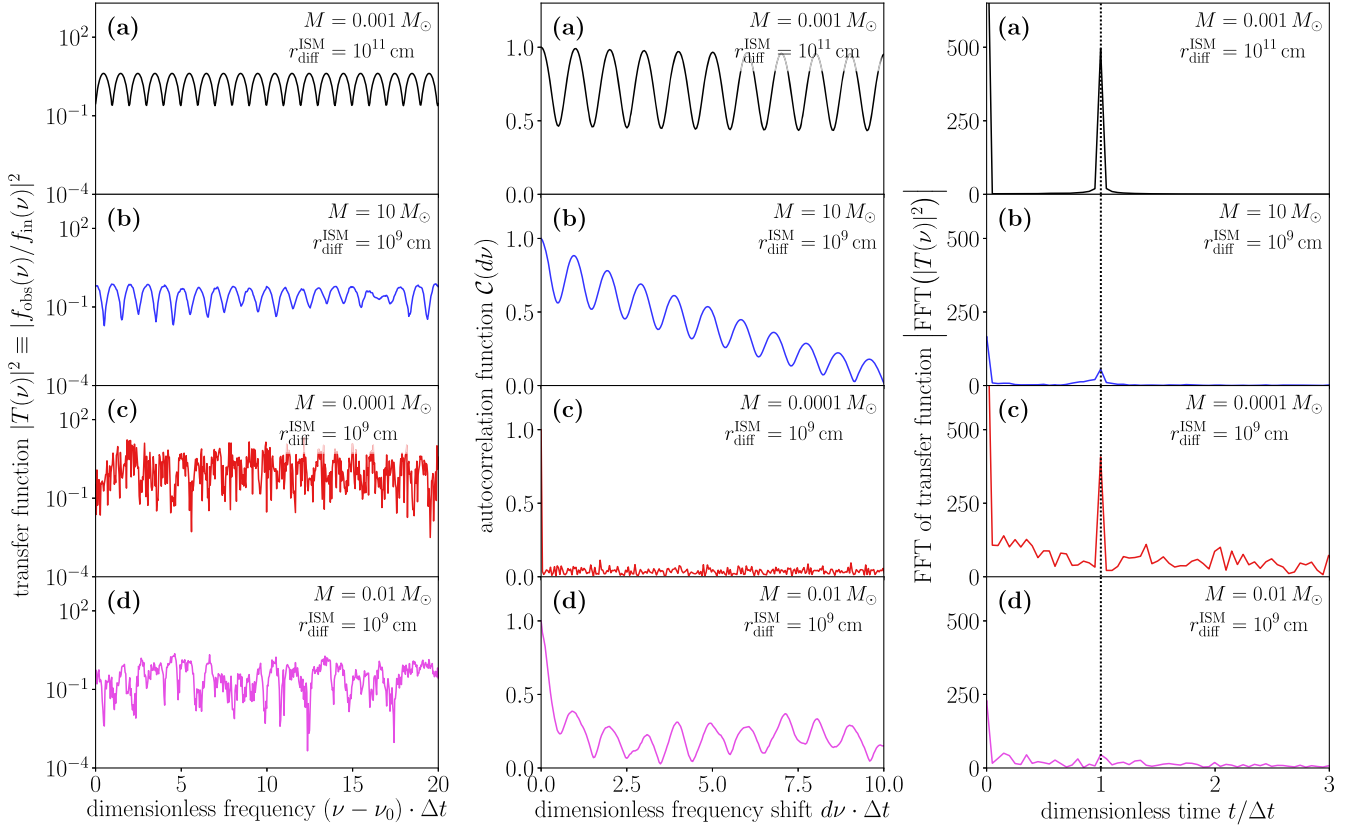
Figure 5. From top to bottom, we illustrate the four qualitatively different scintillation/lensing regimes discussed in the main text. The panels on the left-hand side show in each case the transfer function $|T(\nu)|^2$, that is the observed radiation intensity, normalized to the radiation intensity without lensing and scintillation (see equation 32). In the middle panels we plot the autocorrelation function (equation 33). The panels on the right-hand contain the Fourier transform of $|T(\nu)|^2$, with the lensing peak highlighted by a vertical dotted line. In all panels, the horizontal axis is normalized in terms of the lensing time delay Δt, and we use $\nu_0 = 1$ GHz. Values of r_{diff} are quoted at the midpoint of the spectrum. The plots have been produced using the simulation code described in Section 4 (Katz, Kopp & Xue 2019a), assuming an interstellar scintillation screen at 1 kpc, and a lens at $D_L = D_S/2$, $y = \beta/\theta_E = 0.5$.
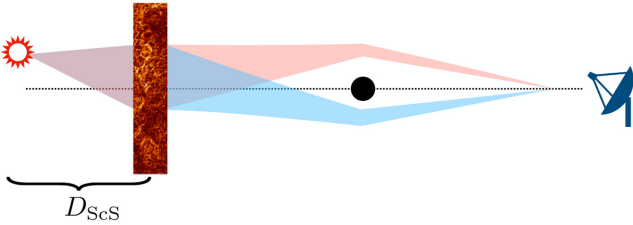

Figure 6. Setup with the scintillation screen between the source and the lens.

with the integral taken along the line of sight. The phase shift has strong frequency dependence and causes a time delay between signals in different frequency bands. In practice, the net time delay due to the average electron density $\bar{n}_e$ is removed by the dedispersion procedure that is typically applied to FRB data. Scintillation is due to a residual phase shift generated by random fluctuations in the electron density $\delta n_e = n_e - \bar{n}_e$.

We assume that on the scales we are interested in the density fluctuations obey statistical homogeneity and isotropy. Hence they are characterized by an isotropic power spectrum related to the

density correlation function as,[7]

$$\langle \delta n_e(\vec{X} + \Delta\vec{X})\, \delta n_e(\vec{X}) \rangle = \int d^3\kappa\, e^{i\vec{\kappa}\Delta\vec{X}}\, P_n(\kappa)\,, \tag{37}$$

Here, $\vec{X} = (\vec{x}, z)$ is a 3D coordinate vector, and $\kappa \equiv |\vec{\kappa}|$. Observations indicate that in a wide range of wavenumbers the power spectrum obeys Kolmogorov-like scaling characteristic of a turbulent behaviour (Armstrong, Cordes & Rickett 1981; Armstrong, Rickett & Spangler 1995),

$$P_n(\kappa) = C_n^2\, \kappa^{-11/3}\,, \qquad \frac{2\pi}{l_{\text{out}}} < \kappa < \frac{2\pi}{l_{\text{in}}}\,. \tag{38}$$

The *outer* scale of interstellar turbulence is estimated to be $l_{\text{out}} \simeq 10 \div 100$ pc and the *inner* scale l_{in} is smaller than 10^8 cm; the level of turbulence is (Elmegreen & Scalo 2004; Scalo & Elmegreen 2004)

$$C_n^2 \simeq (10^{-4} \div 10^{-3})\, \text{m}^{-20/3}\,. \tag{39}$$

---

[7]We use the notation κ for the wavenumber of the fluctuations to distinguish it from the wavenumber of the electromagnetic wave k.

The amplitude of fluctuations with length scale l can be estimated from the power spectrum as

$$\delta n_e\big|_l \sim \left(4\pi \int_0^{2\pi/l} d\kappa \, \kappa^2 P_n(\kappa)\right)^{1/2} \sim (6\pi C_n^2)^{1/2}\left(\frac{l}{2\pi}\right)^{1/3}. \quad (40)$$

Note that the fluctuation amplitude increases with scale and at the outer scale becomes comparable to the mean electron density in the galaxy,

$$\delta n_e\big|_{l_{out}} \sim \bar{n}_e , \quad (41)$$

where $\bar{n}_e = (0.01 \div 0.1)\,\mathrm{cm}^{-3}$ (Cordes & Lazio 2002). The dominant energy source for ISM turbulence is most likely supernova remnants, but other sources like stellar winds or protostellar outflows can also play a role (Elmegreen & Scalo 2004; Shukurov 2011). Even though Kolmogorov scaling (38) is widely used for the description of the turbulent ISM, its origin remains a matter of debate. The original Kolmogorov theory (Kolmogorov 1941a,b) predicts the spectrum of energy fluctuations in the inertial range of an incompressible fluid $P_E(\kappa) \propto \kappa^{-11/3}$. It is not entirely clear why the spectrum of density fluctuations in the compressible ISM should follow the same power law, for a review of existing proposals (see Elmegreen & Scalo 2004). Following the common practice, we will adopt (38) in our estimates.

We can now express the phase structure function $\xi(\omega, r)$ from equation (13) in terms of $P_n(\kappa)$ by plugging the relation (36) between $\varphi(\omega, \vec{x})$ and $n_e(\vec{X})$, as well as the density correlation function equation (37), into equation (13) (Rickett 1990):

$$\xi(\omega, r) = 8\pi^2 L \left(\frac{2\pi\alpha}{m_e\omega}\right)^2 \int_0^\infty d\kappa \, \kappa \, (1 - J_0(\kappa r)) P_n(\kappa). \quad (42)$$

Here, L is the thickness of the ISM layer traversed by the wave and $J_0(z)$ is the Bessel function. Substitution of the Kolmogorov spectrum (38) yields,

$$\xi(\omega, r) = \left(\frac{r}{r_{\mathrm{diff}}(\omega)}\right)^{5/3}, \quad (43)$$

with the diffractive scale

$$r_{\mathrm{diff}} = 0.068 \times (C_n^2 L)^{-3/5}\left(\frac{m_e\omega}{2\pi\alpha}\right)^{6/5}. \quad (44)$$

For the typical thickness of the galactic disc $L \sim 1\,\mathrm{kpc}$ we obtain,

$$r_{\mathrm{diff}} = 4.2 \times 10^9\,\mathrm{cm}\left(\frac{L}{\mathrm{kpc}}\right)^{-3/5}\left(\frac{C_n^2}{10^{-4}\,\mathrm{m}^{-20/3}}\right)^{-3/5}\left(\frac{\nu}{\mathrm{GHz}}\right)^{6/5}. \quad (45)$$

According to Fig. 4, this belongs to the range of values admitting separation of the lensing effects from scintillation. Note a rather steep growth of the diffractive scale with frequency which results in a rapid suppression of scintillation for frequencies above a few GHz.

3.3.2 The intergalactic medium

While turbulence and thus scintillation in the ISM is already fraught with large uncertainties, even less is known about the properties of the IGM. In fact, much of what we know about IGM turbulence comes from observations of FRBs (Macquart & Koay 2013; Cordes et al. 2016; Zhu, Feng & Zhang 2018). While to the best of our knowledge IGM scintillation has not yet been measured experimentally, there are indications that it might be accessible to SKA (Koay & Macquart 2015).
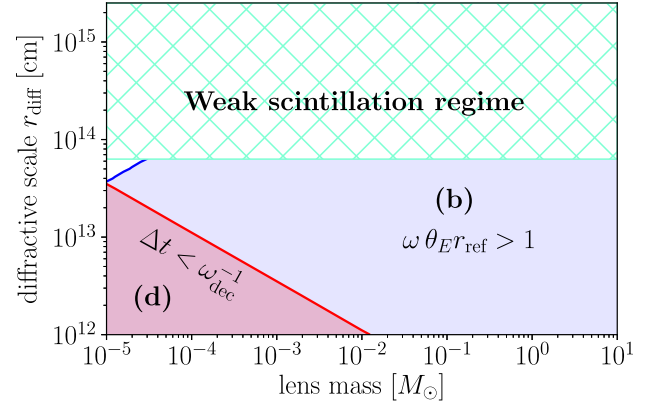

Figure 7. Impact of intergalactic scintillation on FRB lensing by compact objects, shown here as a function of the lens mass M and the diffractive scintillation scale r_{diff}. We assume an FRB at a comoving distance of 1 Gpc, and a lens at 0.5 Gpc. The scintillation screen is placed between the lens and the observer at 0.25 Gpc. The angular separation between the lens and the (unlensed) source, normalized to the Einstein angle, is $y = \beta/\theta_E = 0.5$. The frequency of the radio signal is taken to be 1 GHz.

In the absence of direct measurements, we are forced to rely on theoretical estimates. Assuming Kolmogorov turbulence, we can estimate the magnitude of IGM density fluctuations, C_n^2, by equating the density fluctuation at the outer scale to the average IGM electron density $\bar{n}_e \simeq 2.2 \times 10^{-7}\,\mathrm{cm}^{-3}$, corresponding to fully ionized hydrogen and helium (Koay & Macquart 2015).[8] Considering the balance between heating and dissipation of energy in the IGM, ref. Luan & Goldreich (2014) estimated the outer scale to be of the order of $l_{out} \sim 10^{24}\,\mathrm{cm}$ ($\sim 0.3\,\mathrm{Mpc}$). This leads to

$$C_n^2 \sim 2 \times 10^{-17}\,\mathrm{m}^{-20/3}\left(\frac{\bar{n}_e}{2.2 \times 10^{-7}\,\mathrm{cm}^{-3}}\right)^2\left(\frac{l_{out}}{10^{24}\,\mathrm{cm}}\right)^{-2/3}. \quad (46)$$

Substituting this into equation (45) and normalizing the thickness of IGM to 1 Gpc we obtain the diffractive scale,

$$r_{\mathrm{diff}} \sim 4.5 \times 10^{13}\,\mathrm{cm}\left(\frac{L}{\mathrm{Gpc}}\right)^{-3/5}\left(\frac{l_{out}}{10^{24}\,\mathrm{cm}}\right)^{2/5}$$

$$\times\left(\frac{\bar{n}_e}{2.2 \times 10^{-7}\,\mathrm{cm}^{-3}}\right)^{-6/5}\left(\frac{\nu}{\mathrm{GHz}}\right)^{6/5}. \quad (47)$$

This is comparable to the Fresnel radius for a scintillation screen 0.25 Gpc away, $r_F \simeq 6.3 \times 10^{13}\,\mathrm{cm}$. We conclude that intergalactic scintillation is at the borderline between the weak and strong scintillation regimes.

The observability of the lensing signal in the presence of IGM scintillation is illustrated in Fig. 7 as a function of r_{diff} and of the lens mass. We see that for realistic parameters and most of the interesting values of the lens mass the signal will be in regime (b). In other words, the two lensed images will be distorted incoherently, but the decorrelation bandwidth of the scintillation will be large enough to accommodate multiple lensing fringes.

The above estimate is based on the assumption that there are no baryon overdensities – such as an interjacent galaxy or galaxy

---

[8]For simplicity, we neglect here the effects of redshift. They can be taken into account systematically along the lines of ref. Macquart & Koay (2013).

cluster – along the line of sight. As $r_{\rm diff}$ scales with $\bar{n}_e^{-6/5}$, such an overdensity can greatly increase the strength of the scintillation. While this might offer interesting opportunities for studies of the IGM using scintillation (Ferrara & Perna 2001; Pallottini, Ferrara & Evoli 2013; Koay & Macquart 2015), it is undesirable for searches of FRB diffractive lensing. Fortunately, for sources at small redshifts $z_S < 1$, where most observed FRBs are expected to occur, the probability that the line of sight crosses a major baryon overdensity is low. Namely, the probability of crossing a galaxy cluster is less than 20 per cent and about 3 per cent for galaxies (Macquart & Koay 2013). We will therefore assume the absence of overdensities and use $r_{\rm diff} \sim 4.5 \times 10^{13}$ cm for the IGM.[9]

In a real sample of FRBs, one could use the known locations of galaxies and galaxy clusters along the various lines of sight to reject those FRBs which are likely to be affected by baryon overdensities. Note that this restriction implies that the lens itself cannot lie inside a galaxy or a cluster. This is not a problem for dark matter, most of which is distributed in diffuse haloes, filaments, and voids. On the other hand, it essentially precludes searching for diffractive lensing by compact objects of astrophysical origin, such as brown dwarfs (Eichler 2017).[10]

3.4 Scintillation summary

When studying realistic lensed FRB signals, we should in principle consider the effect of intergalactic scintillation, of interstellar scintillation in the FRB's host galaxy, and of interstellar scintillation in the Milky Way. From the discussion of the previous subsection, we expect the effect of the IGM to be typically less important than that of the ISM. We have verified this using a sample of simulations where we combined IGM scintillation screens with ISM screens (see Section 4 for the description of the simulation code Katz et al. 2019a). However, the numerical cost of the simulations grows rapidly with the number of screens, so to reduce the computation time, we *neglect* IGM scintillation in the rest of our analysis.

The properties of the FRB host galaxies remain largely unknown, despite localization of several burst sources (Chatterjee et al. 2017; Tendulkar et al. 2017; Bannister et al. 2019; Ravi et al. 2019). In the absence of any detailed information, we assume that the properties of the ISM in the host galaxy are similar to that in the Milky Way. Then, barring a chance alignment of the line of sight with the galactic disc of the host, one can assume the scintillation screen of the host galaxy to have similar an effect on the lensing signal as the ISM screen of the Milky Way.[11] Therefore, for our exploratory study of the detectability of FRB lensing we choose to consider only the ISM screen of the Milky Way, which allows us to further reduce the required computing resources. It is worth emphasizing,

however, that an actual future search for lensing signal in the data should include modelling of scintillation both in the host galaxy and in the IGM.

4 SIMULATIONS AND RESULTS

4.1 Formalism

To better understand the effect of scintillation on the spectra of astronomical radio sources in general and FRBs in particular, we have developed a simulation code to describe both lensing and scintillation. It is capable of evolving the signal from a point-like or extended radio source through an arbitrary stack of lensing and scintillation screens, and onwards to an observer. Each screen corresponds to a 2D plane, oriented perpendicular to the line of sight. It associates each point $\vec{x} = (x^1, x^2)$ on the plane with a characteristic phase factor $\varphi_j(\vec{x})$ that is imparted to photons passing through that point on the screen. Here, the index j numbers the successive screens. The photon field $A_j(\vec{x})$ on the j-th screen is obtained from the field $A_{j-1}(\vec{x})$ on the previous screen according to the Fresnel integral,

$$A_j(\vec{x}) = \frac{k\, e^{ik(z_j - z_{j-1})}}{2\pi i (z_j - z_{j-1})} \int d^2x'\, A_{j-1}(\vec{x}')$$
$$\times \exp\left(\frac{ik|\vec{x} - \vec{x}'|^2}{2(z_j - z_{j-1})} + i\varphi_j(\vec{x})\right) \tag{48}$$

(in analogy to equations 11 and 12). Here, z_j is the comoving line-of-sight distance of the source and the j-th screen, and the wavenumber k is given by the dispersion relation in a plasma (equation 34). In evaluating the plasma frequency ω_p, we assume a mean ISM plasma density of $n_e = 0.03\,{\rm cm}^{-3}$. The plasma density in the IGM is several orders of magnitude smaller, but as we neglect scintillation in the IGM following the discussion in Section 3.3, its precise value does not affect our analysis. Without IGM scintillation, there is no multipath propagation through the IGM, so all photons of a given frequency are dispersed by the same amount. The screen $A_0(\vec{x})$ corresponds to the source; for a point-like source, it is simply a δ-function centred at the coordinates $\vec{x}_0$ of the source, $A_0(\vec{x}) = \delta^{(2)}(\vec{x} - \vec{x}_0)$. The last ($n$-th) screen in the stack is placed at the location of the observer, so that the photon field $A_n(\vec{x})$ corresponds to the observed image. We will not consider the spatial extent of the image here and just evaluate $A_n(0)$ for simplicity.

As in Section 3.1, the first term in the exponential factor under the integral in equation (48) describes the additional geometric phase that photons experience when travelling from $\vec{x}'$ to $\vec{x}$ (in the limit that $|\vec{x}| \ll z_j - z_{j-1}$). For lensing screens, the phase factor $\varphi_j(\vec{x})$ describes the non-geometric part of the Shapiro time delay

$$\varphi_j^{\rm lens}(\vec{x}) = -\frac{(z_{j+1} - z_j)(z_{j+1} - z_{j-1})}{z_j - z_{j-1}}\psi(\vec{x})\,, \tag{49}$$

where $\psi(\vec{x}) = \theta_E^2 \log\left[|\vec{x}|/(z_{j+1} - z_{j-1})\right]$ is again the lensing potential for a point-like lens, and θ_E is the Einstein angle defined in equation (3).

For scintillation screens, $\varphi_j(\vec{x}) = \varphi_j^{\rm scint}(\vec{x})$ describes the variation in the dispersion relation due to random fluctuations of the plasma density in the scintillating medium. As discussed in Section 3.3, it is the modelling of these fluctuations that is the main source of uncertainty in our calculations. We assume Kolmogorov turbulence (Kolmogorov 1941a, b; Elmegreen & Scalo 2004), i.e. we assume that the fluctuation mode with wavenumber $\vec{\kappa}$ on the screen has an

---

[9]Note that these estimates are still highly simplified. For instance, they neglect the possibility of turbulent plasma far out in the halo of spiral galaxies. Moreover, our treatment of scintillation does not distinguish between spiral and elliptic galaxies. We do not expect such refinements to qualitatively change our result, and we therefore leave them for future work.

[10]The latter search might still be possible at higher frequencies $\nu \gtrsim 5\,{\rm GHz}$ where the scintillation effects are suppressed and the requirement to avoid baryon overdensities may be relaxed.

[11]Strong temporal broadening of the signal has been observed for some FRBs and is consistent with scattering on dense plasma inhomogeneities. These are likely to occur in the close vicinity of the source Katz (2016), Xu & Zhang (2016), in which case they do not significantly affect the detectability of lensing.

amplitude $|\tilde{f}(\vec{\kappa})|$ drawn from a Gaussian distribution of width[12]

$$\sigma^{\text{scint}}(\vec{\kappa}) = \left(\frac{\vec{\kappa}^2}{\kappa_{\text{diff}}^2} \right)^{11/6} . \qquad (50)$$

Here, $\kappa_{\text{diff}} \equiv 2\pi/r_{\text{diff}}$ is an arbitrarily chosen reference scale. The phase of $\tilde{f}(\vec{\kappa})$ is also a random number, uniformly distributed between 0 and 2π. We emphasize that $\vec{\kappa}$ describes density fluctuations on a scintillation screen and should not be confused with the wavenumber k of the photon field. The scintillation phase $\varphi_j^{\text{scint}}(\vec{x})$ is then proportional to the Fourier transform of $\tilde{f}(\vec{\kappa})$:

$$\varphi_j^{\text{scint}}(\vec{x}) \propto \int d^2\kappa \, e^{i\vec{\kappa}\vec{x}} \, \tilde{f}(\vec{\kappa}) . \qquad (51)$$

The normalization of $\varphi_j^{\text{scint}}(\vec{x})$ is chosen such that $\mathcal{O}(1)$ variations in the phase occur over distance scales of the order of r_{diff},

$$\left\langle \left[\varphi(\vec{x}) - \varphi(\vec{x} + r_{\text{diff}}\hat{n}) \right]^2 \right\rangle = 1 , \qquad (52)$$

where $\langle \cdot \rangle$ denotes averaging over the screen, and $\vec{n}$ is a unit vector, which we choose to be oriented in the x^1 direction.[13]

We assume the incoming amplitude of the radiation at frequency ω to be of the form:

$$f_{\text{in}}(\nu) \propto \exp\left(- \frac{\nu}{200\,\text{MHz}} \right). \qquad (53)$$

This expression is an attempt to roughly fit an observed FRB spectrum from ref. Masui et al. (2015). While we do not claim that our extrapolation to higher frequencies than observed in ref. Masui et al. (2015) is necessarily valid, our further analysis will rely mainly on a reconstruction of the transfer function, largely reducing the uncertainties associated with the exact shape of the FRB spectrum (see Section 4.3).

4.2 Numerical implementation

To compute the Fresnel integral in equation (48) numerically, we employ several simplifications:

(i) As the Fresnel integral on a lensing screen is numerically very badly behaved, we treat lensing analytically. In other words, if the j-th screen is a lensing screen, we evolve the photon field directly from screen $j-1$ to screen $j+1$, multiplying by the appropriate magnification (see equation 19). For the lens masses considered in this paper, we always work in the geometric optics limit, even though our code (released together with this paper; Katz et al. 2019a) is also able to handle the wave optics regime, and switches to it automatically if $\omega(D_L D_S/D_{LS})\theta_E^2 < 10$.

(ii) We discretize scintillation screens, i.e. we evaluate the integrand in equation (48) on a square grid of points, and then evaluate the integral as a simple sum. The size of the screen in both directions is chosen $\gg r_{\text{ref}}$ to make sure the region $|\vec{x}| \lesssim r_{\text{ref}}$, from which most of the signal is received, is well within the simulated region. (At distances $\gg r_{\text{ref}}$ from the line of sight, the geometric phase varies much faster than the scintillation phase, so that photons emitted from

this regions mostly interfere destructively.) The grid spacing $\text{d}x$ is chosen much smaller than r_{diff} to make sure the phase fluctuations on the screen are well resolved. Moreover, we require $\text{d}x$ to be small enough to still resolve the fast-varying geometric phase at the edges of the screen. (The last requirement is dropped when the grid becomes so large that it would not fit into GPU memory any more.) To further optimize memory consumption, we do not simulate the whole screen at once. Instead, we first simulate the long wavelength fluctuations, discretized with a coarser grid spacing. The geometric phase factor in the Fresnel integral from equation (48) is evaluated only once for each cell on this coarse grid. The cell size of the coarse grid is chosen $\ll r_F$ to ensure that this is a good approximation. For simulating shorter wavelength fluctuations, we divide the screen into smaller patches and simulate the fluctuations on each of them separately, but at full resolution $\text{d}x$. The patches are always chosen much larger than r_{diff}.

(iii) For most of our results, we reduce the scintillation screen to one dimension. In other words, we assume all photons to travel in the x^1–z plane. This greatly reduces memory consumption and computational effort, while all the essential features of scintillation are preserved, as evidenced by the good agreement with the qualitative analytic estimates from Section 3.2.

Our code (Katz et al. 2019a) is written in PYTHON 3, making heavy use of the CUPY library Okuta et al. (2017) to run it on CUDA-enabled GPUs and thus optimally benefit from the vectorizability and scalability of our approach. In order to vectorize the evaluation of the magnification function for gravitational lensing in the wave optics regime, we had to implement vectorized versions of certain special functions, notably the gamma function $\Gamma(z)$ and the Laguerre polynomials $L_n(z)$, for the case of complex z and n. In implementing the Gamma function, we follow Lanczos' approximation (Lanczos 1964; Press et al. 1988), while our implementation of the Laguerre polynomials is based on the implementation in the MPMATH package (Johansson et al. 2013, see also Johansson 2016).

4.3 Data analysis

Let us now outline the procedure we use to extract the lensing signal from our simulated data. Our objective is to identify the periodic modulation of the frequency spectrum due to lensing on top of the stochastic background from scintillation. We would like to work in particular with the Fourier transform

$$|\mathcal{T}(\tau)| \equiv \left| \text{FFT}\left(|T(\nu)|^2 \right) \right| \qquad (54)$$

of the transfer function, equation (32), where the lensing signal materializes as a peak at $\tau = \Delta t$. Of course, we do not have direct access to the transfer function and its Fourier transform as we do not know the initial spectrum at the source. Moreover, observing the lensing peak is complicated by the fact that it is typically located on top of a steeply falling (or rising) background.

The first step in our analysis chain is a fit of the logarithm of the 'observed' radiation intensity, $\log I_{\text{obs}}(\nu) \equiv \log |f_{\text{obs}}(\nu)|^2$ with a high-order polynomial (we use $d = 15$). To ensure the fit is smooth, we use polynomial lasso regression with regularization parameter 0.05 (Santosa & Symes 1986; Tibshirani 1996). We then subtract the fit function from $\log I_{\text{obs}}(\nu)$ to obtain an estimate $\log |\hat{T}(\nu)|^2$ of the log of the transfer function $|T(\nu)|^2$ (equation 32). Besides lasso regression with a 15th order polynomial, we tried several alternative fitting functions and regularization methods (for instance ridge regression). We found them to all perform roughly comparably. The minor effects that various fitting strategies might induce on the

---

[12]In general the statistics of the scintillation phase may be non-Gaussian. A study of the corresponding effects is, however, beyond the scope of this paper.

[13]This choice is convenient, given our discretization of the scintillation screen. In principle, we should average over all directions of $\vec{n}$, but doing so would not significantly affect our results because of the statistical isotropy of the screen.

reconstructed spectrum, can be studied by the reader independently using our public code (Katz et al. 2019a).

At the second stage of our analysis, we look for peaks in $|\mathcal{T}(\tau)|$, defined in equation (54). For a fixed peak time delay τ_0 and peak width w_τ, we fit a polynomial $P(\tau_0, w_\tau; \tau)$ to the Fourier power spectrum (in linear space), excluding the points in the interval $[\tau_0 - w_\tau/2, \tau_0 + w_\tau/2)$. The fitting is performed by polynomial ridge regression, with regularization parameter 10^{-4}. As previously, fitting with other parameters yields comparable results and the small differences can be traced by using alternative methods in our code (Katz et al. 2019a). We then define a test statistic $\hat{\sigma}$ as the difference between $|\mathcal{T}(\tau)|^2$ at the peak and the polynomial at this time delay, normalized by the width of the peak and by the standard deviation of all samples outside the peak region:

$$\hat{\sigma}(\tau_0, w_\tau) = \frac{N_{\text{out peak}} \sum_{j \text{ in peak}} \left(|\mathcal{T}(\tau)|^2 - P(\tau_0, w_\tau; \tau)\right)}{N_{\text{in peak}} \sum_{j \text{ outside peak}} \left||\mathcal{T}(\tau)|^2 - P(\tau_0, w_\tau; \tau)\right|}. \quad (55)$$

Here the sum in the numerator runs over the N time delay samples inside the peak region, while the sum in the denominator runs over all samples outside the peak region. We repeat this procedure for each time delay τ_0 and each width w_τ, and we consider as a potentially interesting peak any local maximum in the 2D manifold defined by $\hat{\sigma}(\tau_0, w_\tau)$. We quote a non-zero test statistic for the lensing signal if a peak is found located within 15 per cent from the 'real' Δt of the lens. Otherwise, we set $\hat{\sigma} = 0$. Note that the lensing peak is typically narrow, so the highest significance is always found for the minimum value of w_τ, which corresponds to a peak spanning two time delay bins. The procedure is illustrated in Fig. 8.

In the right-hand column of that figure, we also show how the lensing peak in $|\mathcal{T}(\tau)|^2$ is affected if we average $I_{\text{obs}}(\nu)$ over frequency intervals $\Delta\nu_{\text{av}} = 17$ MHz before taking the Fourier transform. We see that high-τ fluctuations are suppressed, but also the height of the lensing peak is somewhat reduced. Averaging is therefore a useful tool only when high-τ fluctuations are worrisome. In our subsequent analysis, we will not use averaging.

To translate the test statistic $\hat{\sigma}$ into a statistical significance, which can then be interpreted as a quantile of the normal distribution, we have simulated 10 000 pseudo-experiments. Each of them corresponds to an unlensed FRB distorted by a scintillation screen with $r_{\text{diff}} = 10^{10}$ cm at 1 kpc. In each pseudo-experiment, we look for a spurious peak at the Δt that would correspond to lensing by a 10^{-3} $M_\odot$ PBH located at $D_L = 0.5$ Gpc, $y = 0.5$. We plot the distribution of the $\hat{\sigma}$ values of the spurious peaks in Fig. 9. The quantiles of this distribution correspond to the real statistical significance σ, which we will use below to set limits on the PBH abundance.

One comment is in order regarding this calibration procedure. The distribution of $\hat{\sigma}$ values can depend on the diffractive scale r_{diff} of the scintillation screen. Nonetheless, as generating a large number of pseudo-experiments is computationally expensive, we use the curve in Fig. 9 for all values of r_{diff}. For $r_{\text{diff}} > 10^{10}$ cm, applying calibration based on Fig. 9 is too conservative, while for smaller r_{diff}, it may somewhat overestimate the sensitivity. However, we are going to find that for $r_{\text{diff}} \sim 10^9$ cm, the sensitivity is weak anyway.

4.4 Results

To anticipate the sensitivity of FRB lensing to compact dark matter objects, we now investigate the significance of the lensing signal as a function of the model parameters, in particular the lens mass M, its position D_L along the line of sight and angular distance β

from the line of sight, as well as the diffractive scintillation scale r_{diff} in the Milky Way. For simplicity, we will keep the distance of the source fixed at 1 Gpc (comoving), we will neglect intergalactic scintillation as well as scintillation in the FRB's host galaxy, and we will assume the Milky Way's scintillation screen to be located at a distance of 1 kpc.

As a first result, we show in Fig. 10 the local statistical significance of the lensing signal as a function of M and r_{diff}, keeping $D_S = 1$ Gpc, $D_L = 0.5$ Gpc, and $y \equiv \beta/\theta_E = 0.5$ fixed. Note that in this scan we choose the instrumental frequency band and frequency resolution as needed to well resolve the lensing peak. This assumption may be unrealistic at very small lens masses, which require very large frequency bands, and at very large lens masses, which require very high frequency resolution. Therefore, at high and low lens masses Fig. 10 should be thought of as proof of principle rather than as a realistic expectation. Fig. 10 confirms our expectations from Fig. 4: the sensitivity is good except at the smallest r_{diff} values. In the left-hand panel of Fig. 10, we observe a loss of sensitivity at low masses. There, the lensing peak in $|\mathcal{T}(\tau)|^2$ falls in the low-τ region and is buried underneath the Fourier transform of the smooth component of the intensity spectrum. As expected, reconstruction of the transfer function by dividing out the smooth component significantly increases the sensitivity, as illustrated in the right-hand panel.

In order to proceed further, we focus specifically on a future SKA-type observatory.[14] This is expected to have a wide frequency band extending above a few GHz. Going to higher frequencies is beneficial for detecting diffractive lensing by dark matter as it makes scintillation less important. Of course, our analysis can be repeated for radiotelescopes operating at lower frequencies, in particular, for CHIME[15] and ASKAP.[16]

As our fiducial parameters we will assume a frequency resolution no better than 1 MHz and a band width no larger than 10 GHz. This is based on the frequency range of the SKA-MID array, and on the expected resolution of the instrument Dewdney et al. (2015), Bonaldi & Braun (2018). With these assumptions, we simulate the lensing signal as a function of the lens mass, the lens distance D_L from the observer, and its angular distance y from the line of sight. Once again, we assume $D_S = 1$ Gpc, and we introduce an interstellar scintillation screen at 1 kpc, with $r_{\text{diff}} = 10^{10}$ cm. For each combination of M, D_L, and y, we then estimate the expected local significance of the signal, as described in Section 4.3. Note that we do not run simulations for lens masses above 0.1 $M_\odot$ because detecting a lensing signal in that case would require a frequency resolution better than 1 MHz. Similarly, we do not consider lens masses below 10^{-4} $M_\odot$, where the spacing of lensing fringes in the spectrum becomes comparable to the maximum bandwidth.

To obtain a bound on the abundance of point-like lenses such as PBHs, we largely follow the statistical procedure described in Katz et al. (2018). We define the likelihood function for a single FRB source at redshift Z_S,

$$L_{\text{FRB}}(M, \rho_{\text{PBH}}, Z_S) = L_0(0) + \int d^3x \, (1 + Z_L)^3 \frac{\rho_{\text{PBH}}}{M} \left[L_0(\vec{\mu}) - L_0(0)\right]. \quad (56)$$

Here, $L_0(\vec{\mu})$ is the likelihood of the (simulated) data – assumed not to contain a lensing signal – when compared to a model that does contain a lens with parameters $\vec{\mu} \equiv (M, Z_L, y)$. We set $L_0(\vec{\mu}) = 1 - \text{erf}(\sigma/\sqrt{2})$, where σ is the significance of the lensing

---

[14]https://www.skatelescope.org
[15]https://chime-experiment.ca
[16]https://www.atnf.csiro.au/projects/askap/index.html.

$$M = 0.001\,M_\odot, \quad r_{diff} = 10^9\,\text{cm}, \quad y = 0.5, \quad D_L = 0.5\,\text{Gpc}$$
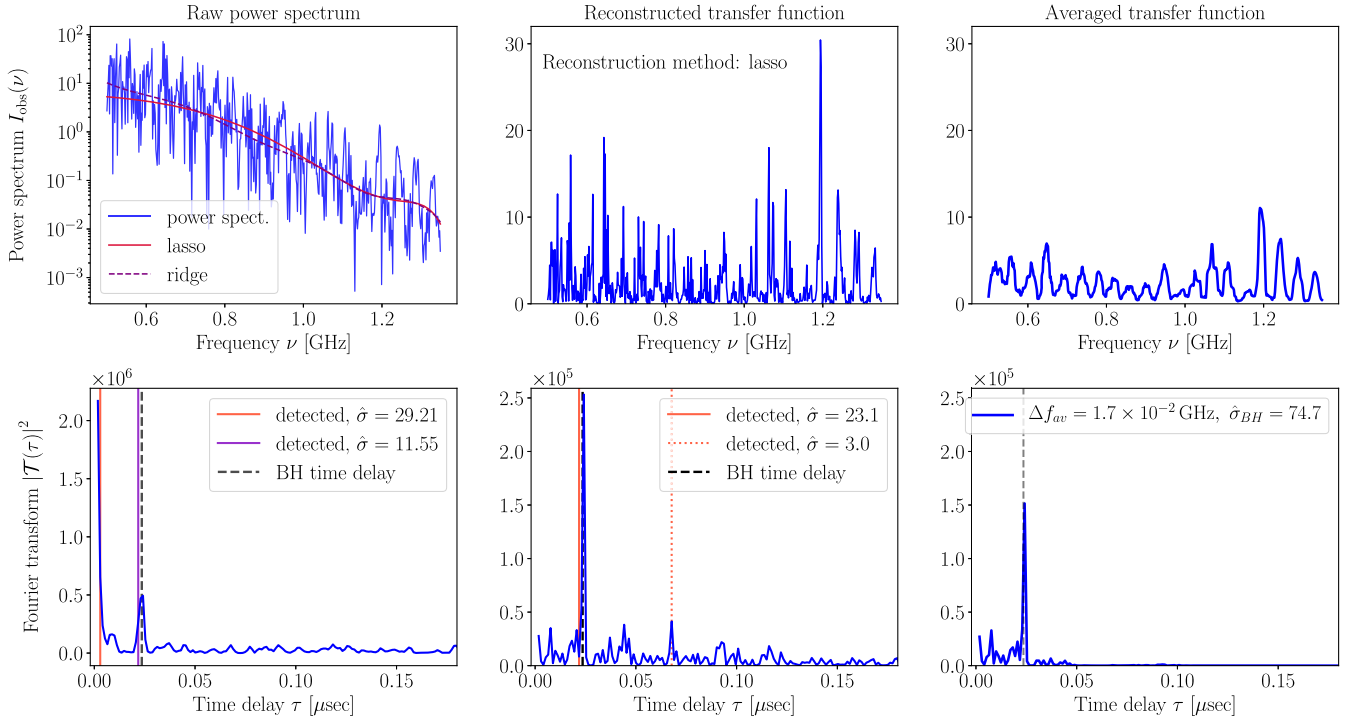

Figure 8. The analysis of a single, diffractively lensed FRB spectrum following the steps described in the text. The upper left-hand plot shows the radiation power spectrum, and the lower left-hand plot shows the Fourier transform thereof, where the lensing peak is clearly visible at the expected time delay (vertical black line). However, we also notice a strong enhancement of the power at small τ, which in some cases spoils the detectability of the lensing peak. Similarly, the middle column shows the reconstructed transfer function and its Fourier transform, and the column on the right-hand side shows the same after averaging procedure described in the text. The enhancement at small τ has disappeared and only the lensing peak remains. We have assumed a source at a comoving distance $D_S = 1$ Gpc and a lens at $D_L = 0.5$ Gpc, $y = 0.5$. An ISM scintillation screen is placed at $D_{ScO} = 1$ kpc, and $r_{diff} = 10^9$ cm at the spectral midpoint.
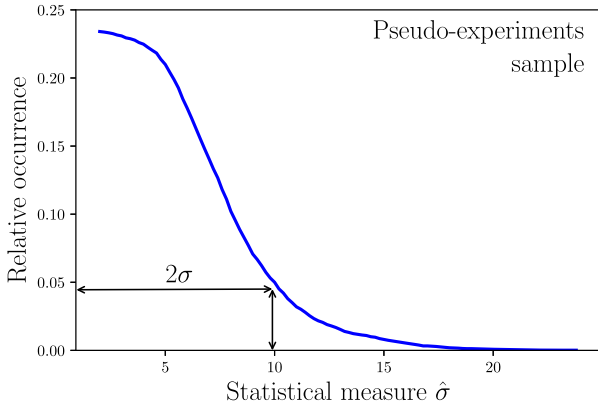

Figure 9. Relative occurrence of statistical measures $\hat{\sigma}$ in the FFT-squared of the power spectrum in the pseudo-experiments sample. The distribution can be reasonably approximated by Gaussian. We calibrate our statistical significance based on this curve.

signal discussed in Section 4.3 above. This immediately implies that $L_0(0)$, the likelihood of the data when compared to the theoretical prediction in the absence of a lens, equals unity. $L_{\text{FRB}}(M, \rho_{\text{PBH}}, Z_S)$ then measures the likelihood of data which does not contain a lensing signal when compared to the prediction assuming a population of lenses of mass M and mass density ρ_{PBH}. The factor $d^3x\,(1 + Z_L)^3\,\rho_{\text{PBH}}/M$ measures the probability of finding a lens in a small volume element d^3x at redshift Z_L. The integral in equation

(56) runs from the source to the observer in the longitudinal (z) direction, and out to infinity in the transverse direction. (In practice, we cut it off at $y = |\vec{x}_\perp|/(D_L \theta_E) = 5$, as there will be no sensitivity to lenses that are further away from the line of sight.) Note that $\vec{x}$ here refers to a 3D physical (not comoving) coordinate. In writing down equation (56), we have assumed that the probability for a single source to be lensed by two lenses simultaneously is negligible.

To compute $L_{\text{FRB}}(M, \rho_{\text{PBH}}, Z_S)$ for a given lens mass M, lens density ρ_{PBH}, and source redshift Z_S, we evaluate σ as function of the lens coordinates. We then evaluate the integral over d^3x on the resulting grid.

Of course, observing just a single FRB is not sufficient to set a meaningful limit on compact dark matter. Observing a large number N of them, however, will greatly boost the sensitivity of the method. We estimate the expected 95 per cent confidence level exclusion limit on ρ_{PBH} for fixed M by solving the equation

$$-2 \log \left(\prod_{i=1}^{N} \frac{L_{\text{FRB}}^i(M, \rho_{PBH}, Z_S^i)}{L_{\text{FRB}}^i(0, 0, Z_S^i)} \right) = 5.99. \tag{57}$$

Note that $L_{\text{FRB}}^i(0, 0, Z_S^i) = 1$. For simplicity, we will in the following assume that all sources are at the same redshift, and that also the properties of the interjacent scintillation screens are the same. When the probability for lensing a single FRB is small ($L_{\text{FRB}}(M, \rho_{\text{PBH}}, Z_S^i) \approx 1$), the reach for the PBH density ρ_{PBH} is then inversely proportional to the number of sources N. This is

Raw power spectrum, $y = 0.5$, $D_L = 0.5$ Gpc

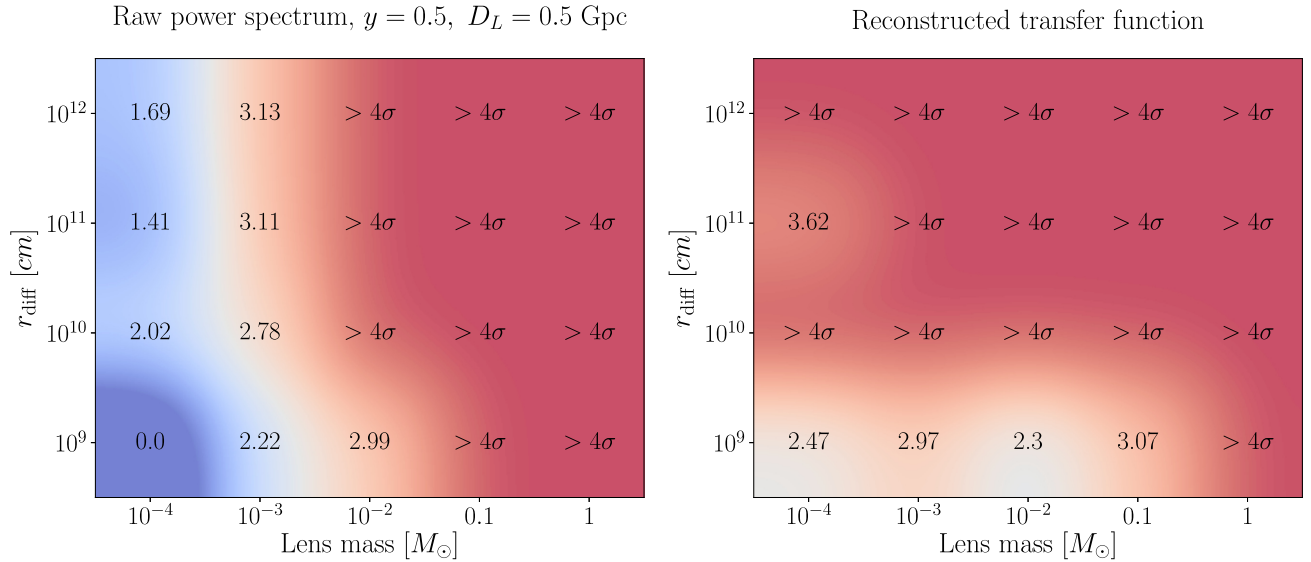Reconstructed transfer function

Figure 10. The local statistical significance of the diffractive lensing signal expected in a typical FRB spectrum as a function of the lens mass M and the diffractive scintillation scale $r_{\rm diff}$ of the interstellar medium. We assume an FRB at a comoving distance of 1 Gpc and a lens at $D_L = 0.5$ Gpc, $y = 0.5$. An ISM scintillation screen is placed at $D_{\rm ScO} = 1$ kpc, and the quoted $r_{\rm diff}$ values are at the spectral midpoint. Numbers in each grid cell indicate the local significance of the scintillation peak in our simulations, calculated as described in Section 4.3. The left-hand panel is based directly on the simulated radiation intensity spectrum, while in the one on the right, we have divided out the smooth component of the spectrum using lasso regression. A clear benefit of this step is visible, especially at low lens masses.

because increasing the number of sources linearly decreases the effective optical depth.

The resulting bound on the PBH parameter space is shown in Fig. 11 and compared to other constraints on primordial black holes. We see that, for a realistic number of FRB observations in SKA (a few tens per day; Macquart et al. 2015), our method can be expected to yield highly competitive constraints. Even more importantly, the expected limits are complementary to those from microlensing searches because FRBs probe the distribution of dark matter over cosmological distance scales, while microlensing is sensitive to dark matter in the Milky Way and its immediate vicinity. This makes diffractive lensing of FRBs a particularly interesting probe for compact dark matter minihaloes, which may be inaccessible to microlensing searches due to their non-negligible spatial extent (Dror et al. 2019). Indeed, the condition $r_L < r_E$ on the lens size r_L, under which the lens can be treated as point-like, is more readily satisfied at cosmological distances. Besides, minihaloes may exist in regions of low baryon density, but may have suffered tidal disruption in the Milky Way. The sensitivity of diffractive lensing ends at PBH masses below $10^{-4}\,\mathrm{M}_\odot$ because at such low masses the lensing peaks in the frequency spectrum are too far apart for a significant number of them to be contained in a realistic instrumental frequency band. At high PBH mass, the limiting factor is the instrumental frequency resolution.

In general, it should be mentioned, that in vast majority of the models the mass distribution of the dark matter can be relatively broad. While we are assuming here a very narrow distribution, generalization to realistic mass distributions is desirable (Green 2016; Carr et al. 2017; Kuhnel & Freese 2017; Bellomo et al. 2018; Laha 2018; Poulter et al. 2019).

Finally, we briefly mention other proposals for probing PBHs in the mass range between $10^{-4}\,\mathrm{M}_\odot$ and $1\,\mathrm{M}_\odot$. A novel method to probe compact objects in the Milky Way is pulsar timing (Siegel, Hertzberg & Fry 2007; Seto & Cooray 2007; Kashiyama & Seto 2012; Clark, Lewis & Scott 2016; Schutz & Liu 2017; Dror

et al. 2019). An alternative, indirect, approach involves primordial gravitational waves produced by adiabatic density fluctuations which also give rise to PBH formation (Saito & Yokoyama 2009; Garcia-Bellido, Peloso & Unal 2017; Cai, Pi & Sasaki 2019). The method is thus specific to PBH production via enhanced adiabatic Gaussian density fluctuations.[18] At somewhat larger PBH masses, one can look for gravitational waves from PBH mergers (Raidal, Vaskonen & Veermae 2017; Kavanagh, Gaggero & Bertone 2018; Abbott et al. 2019; Chen & Huang 2019). The expected gravitational wave signal is, however, subject to large uncertainties in the evolution of PBH populations over cosmological history (Nakamura et al. 1997; Ioka et al. 1998; Ali-Haïmoud, Kovetz & Kamionkowski 2017; Kavanagh et al. 2018; Raidal et al. 2019; Vaskonen & Veermae 2020). In the region of lighter masses, PBHs can lead to the destruction of neutron stars (Capela, Pshirkov & Tinyakov 2013) and white dwarfs (Graham, Rajendran & Varela 2015). Exploiting these mechanisms to set limits is, however, complicated by uncertainties in the dark matter concentration in globular clusters (Conroy, Loeb & Spergel 2011; Ibata et al. 2013) and in the treatment of energy deposition by PBHs crossing stars (Katz, Kurkela & Soloviev 2019b; Montero-Camacho et al. 2019).

5 CONCLUSIONS AND OUTLOOK

In this work we have analysed the sensitivity of diffractive gravitational lensing of FRB signals to compact dark matter objects (MACHOs). Diffractive lensing (sometimes called femtolensing or nanolensing in the literature) means the interference of the two

---

[18]Recently, this method has been applied to NANOGrav data (Chen, Yuan & Huang 2019). However, the resulting limits are exponentially sensitive to theoretical uncertainties.
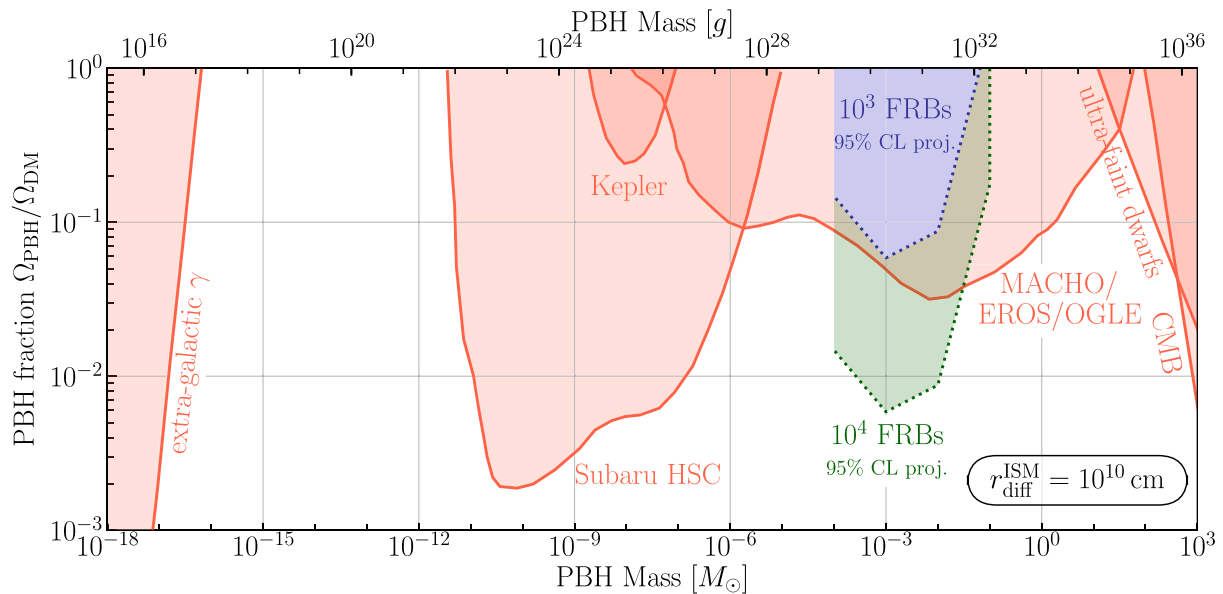
Figure 11. Expected limits on primordial black holes from diffractive lensing of FRBs. We assume an interstellar scintillation screen at a distance of 1 kpc, with diffractive scale $r_{\text{diff}}^{\text{ISM}} = 10^{10}$ cm at 1 GHz, and negligible intergalactic scintillation. We compare our projections (in blue) to microlensing constraints from Subaru HSC (Kepler Griest, Cieplak & Lehner 2013; Niikura et al. 2019),[17] MACHO (Allsman et al. 2001), EROS (Tisserand et al. 2007), and OGLE (Wyrzykowski et al. 2011), to CMB constraints due to accretion on to PBHs (Ali-Haimoud & Kamionkowski 2017), to limits based on the dynamics of ultrafaint dwarf galaxies (Brandt 2016), and to bounds on the contribution of Hawking radiation from PBHs to the extragalactic gamma background (Carr et al. 2010). We emphasize that CMB and gamma-ray background constraints are based on specific properties of PBHs, and that the other existing constraints probe the *local* distribution of dark matter in the Milky Way and its immediate neighbourhood. By contrast, diffractive lensing of FRBs offers a model-independent probe of MACHOs at cosmological distances.

lensed images of a source, which leads to periodic modulation of the observed frequency spectrum.

We have studied the interplay between the lensing signal and distortions caused by interstellar scintillation, and we have concluded that the lensing signal can often be extracted in spite of the distortion. We have developed a data analysis procedure to extract the lensing signal and showed its efficiency on simulated data. Our results indicate that the existing and future FRB surveys carried out by ASKAP, CHIME, and SKA will be able to strongly constrain the cosmological MACHO abundance. As an illustration, we studied the sensitivity of an SKA-like survey to PBH dark matter. We concluded that it will be able to probe the parameter space of PBHs in the mass range between $10^{-4} \, \text{M}_\odot$ and $0.1 \, \text{M}_\odot$ and constrain their abundance down to about 1 per cent of the total dark matter content of the Universe.

Compared to microlensing searches, which also probe primordial black holes in this mass range, our method is unique because it tests the distribution of dark matter at cosmological distances rather than in our local cosmic neighbourhood. This distinction is particularly important when generalizing our bounds to other compact dark matter candidates such as dark matter minihaloes. The local abundance of dark matter minihaloes may be reduced due to tidal disruption in the Milky Way, suppressing the probability of microlensing events. Moreover, microlensing searches may be insensitive to dark matter minihaloes due to their non-negligible spatial extent, which is larger than the Einstein radius at galactic distances. At cosmological scales, on the other hand, the Einstein radius is significantly larger and may well exceed the minihalo's size, so that it acts effectively as a point-like lens. In this case, our results are directly applicable. Investigating the sensitivity of FRB lensing to more extended compact objects will be an interesting direction for future work.

Apart from dark matter, the range of lens masses considered in this paper may also contain objects of astrophysical origin, such as brown dwarfs. However, it appears unlikely that they can produce a discernible lensing signal in FRB spectra. The reason is that they are expected to reside in regions of high baryonic density, namely galaxies, characterized also by high concentrations of free electrons. The scattering of radio waves produced by this ambient plasma will be much stronger than the deflection of light due to gravitational lensing, so that the effect of the latter will be completely swamped by scintillation. In principle, the situation might improve for FRBs with spectra extending to high frequencies $\gtrsim 5$ GHz, where the scintillation effects become weaker. We leave the study of this interesting possibility for future.

Before concluding, we emphasize again that the reach of diffractive lensing of radio signals depends on our understanding of interstellar and intergalactic scintillation, and thus of turbulence in the ISM and IGM. While the scintillation parameters we have assumed in this work represent our current best understanding of these phenomena, future observations should allow us to much better quantify the impact of scintillation. The rapid progress in the study of FRBs and in radio observations in general will contribute to reducing this uncertainty.

ACKNOWLEDGEMENTS

REFERENCES

Abbott B. P. et al., 2019, Phys. Rev. Lett., 123, 161102

Ali-Haïmoud Y., Kamionkowski M., 2017, Phys. Rev. D, 95, 043534

Ali-Haïmoud Y., Kovetz E. D., Kamionkowski M., 2017, Phys. Rev. D, 96, 123523

Allsman R. A. et al., 2001, ApJ, 550, L169

Arbey A., Auffinger J., Silk J., 2020, Phys. Rev. D, 101, 023010

Armstrong J. W., Cordes J. M., Rickett B. J., 1981, Nature, 291, 561

Armstrong J. W., Rickett B. J., Spangler S. R., 1995, ApJ, 443, 209

Ballesteros G., Coronado-Blázquez J., Gaggero D., 2019, preprint (arXiv: 1906.10113)

Bannister K. W. et al., 2019, Science, 365, 565

Barnacka A., Glicenstein J.-F., Moderski R., 2012, Phys. Rev. D, 86, 043001

Bartelmann M., 2010, Class. Quantum Gravity, 27, 233001

Bellomo N., Bernal J. L., Raccanelli A., Verde L., 2018, J. Cosmol. Astropart. Phys., 2018, 004

Berezinsky V., Dokuchaev V., Eroshenko Y., 2006, Phys. Rev. D, 73, 063504

Berezinsky V. S., Dokuchaev V. I., Eroshenko Y. N., 2014, Phys. Usp., 57, 1 [Usp. Fiz. Nauk, 184, 3 (2014)]

Bonaldi A., Braun R., 2018, preprint (arXiv:1811.10454)

Boudaud M., Cirelli M., 2019, Phys. Rev. Lett., 122, 041104

Brandt T. D., 2016, ApJ, 824, L31

Buschmann M., Foster J. W., Safdi B. R., 2020, Phys. Rev. Lett., 124, 161103

Cai R.-g., Pi S., Sasaki M., 2019, Phys. Rev. Lett., 122, 201101

Capela F., Pshirkov M., Tinyakov P., 2013, Phys. Rev. D, 87, 123524

Carr B. J., Kohri K., Sendouda Y., Yokoyama J., 2010, Phys. Rev. D, 81, 104019

Carr B., Kühnel F., Sandstad M., 2016, Phys. Rev. D, 94, 083504

Carr B., Raidal M., Tenkanen T., Vaskonen V., Veermäe H., 2017, Phys. Rev. D, 96, 023514

Chatterjee S. et al., 2017, Nature, 541, 58

Chawla P. et al., 2017, ApJ, 844, 140

Chen Z.-C., Huang Q.-G., 2019, preprint (arXiv:1904.02396)

Chen Z.-C., Yuan C., Huang Q.-G., 2019, preprint (arXiv:1910.12239)

Clark H. A., Lewis G. F., Scott P., 2016, MNRAS, 456, 1394 [Erratum: MNRAS464,no.2,2468(2017)]

Conroy C., Loeb A., Spergel D., 2011, ApJ, 741, 72

Cordes J. M., Lazio T. J. W., 2002, preprint (astro-ph/0207156)

Cordes J. M., Wharton R. S., Spitler L. G., Chatterjee S., Wasserman I., 2016, preprint (arXiv:1605.05890)

Dai L., Lu W., 2017, ApJ, 847, 19

Dasgupta B., Laha R., Ray A., 2019, preprint (arXiv:1912.01014)

DeRocco W., Graham P. W., 2019, Phys. Rev. Lett., 123, 251102

Dewdney P. et al., 2015, Technical Report SKA-TEL-SKO-0000308, SKA1 System Baseline V2 Description. Macclesfield, Cheshire, UK

Dokuchaev V. I., Eroshenko Yu. N., Tkachev I. I., 2017, J. Exp. Theor. Phys., 125, 434 [Zh. Eksp. Teor. Fiz.152,no.3,511(2017)]

Dror J. A., Ramani H., Trickle T., Zurek K. M., 2019, Phys. Rev. D, 100, 023003

Eggemeier B., Redondo J., Dolag K., Niemeyer J. C., Vaquero A., 2019, preprint (arXiv:1911.09417)

Eichler D., 2017, ApJ, 850, 159

Elmegreen B. G., Scalo J., 2004, ARA&A, 42, 211

Fairbairn M., Marsh D. J. E., Quevillon J., Rozier S., 2018, Phys. Rev. D, 97, 083502

Ferrara A., Perna R., 2001, MNRAS, 325, 1643

García-Bellido J., Peloso M., Unal C., 2017, J. Cosmol. Astropart. Phys., 2017, 013

Goerdt T., Gnedin O. Y., Moore B., Diemand J., Stadel J., 2007, MNRAS, 375, 191

Gould A., 1992, ApJ, 386, L5

Graham P. W., Rajendran S., Varela J., 2015, Phys. Rev. D, 92, 063007

Green A. M., 2016, Phys. Rev. D, 94, 063530

Green A. M., Goodwin S. P., 2007, MNRAS, 375, 1111

Griest K., Cieplak A. M., Lehner M. J., 2013, Phys. Rev. Lett., 111, 181302

Hardy E., 2017, J, High Energy Phys., 02, 046

Hawking S., 1971, MNRAS, 152, 75

Hogan C. J., Rees M. J., 1988, Phys. Lett. B, 205, 228

Ibata R., Nipoti C., Sollima A., Bellazzini M., Chapman S., Dalessandro E., 2013, MNRAS, 428, 3648

Ioka K., Chiba T., Tanaka T., Nakamura T., 1998, Phys. Rev. D, 58, 063003

Johansson F., 2016, CoRR, preprint (arXiv:1606.06977)

Johansson F. et al., 2013, mpmath: a Python library for arbitrary-precision floating-point arithmetic (version 0.18). Available at: http://mpmath.org/

Kashiyama K., Seto N., 2012, MNRAS, 426, 1369

Katz J. I., 2016, ApJ, 818, 19

Katz J. I., 2018, Prog. Part. Nucl. Phys., 103, 1

Katz A., Kopp J., Sibiryakov S., Xue W., 2018, J. Cosmol. Astropart. Phys., 2018, 005

Katz A., Kopp J., Xue W., 2019a, GitHub repository. Available at: https://github.com/andrey-katz/FRB_lensing

Katz A., Kurkela A., Soloviev A., 2019b, J. Cosmol. Astropart. Phys., 1908, 017

Kavanagh B. J., Gaggero D., Bertone G., 2018, Phys. Rev. D, 98, 023536

Koay J. Y., Macquart J.-P., 2015, MNRAS, 446, 2370

Kolb E. W., Tkachev I. I., 1993, Phys. Rev. Lett., 71, 3051

Kolb E. W., Tkachev I. I., 1994, Phys. Rev. D, 49, 5040

Kolmogorov A., 1941a, Akad. Nauk SSSR Dokl., 30, 301

Kolmogorov A. N., 1941b, Akad. Nauk SSSR Dokl., 32, 16

Kuhnel F., Freese K., 2017, Phys. Rev. D, 95, 083508

Laha R., 2018, preprint (arXiv:1812.11810)

Lanczos C., 1964, J. Soc. Industr. Appl. Math. B , 1, 86

Li Z.-X., Gao H., Ding X.-H., Wang G.-J., Zhang B., 2018, Nature Commun., 9, 3833

Lorimer D., Kramer M., 2005, Handbook of Pulsar Astronomy. Cambridge Univ. Press, Cambridge

Luan J., Goldreich P., 2014, ApJ, 785, L26

Macquart J. P. et al., 2015, Proc. Sci., Fast Transients at Cosmological Distances with the SKA. SISSA, Trieste, PoS(AASKA14)055

Macquart J.-P., Koay J.-Y., 2013, ApJ, 776, 125

Masui K. et al., 2015, Nature, 528, 523

Matsunaga N., Yamamoto K., 2006, J. Cosmol. Astropart. Phys., 2006, 023

Moniez M., 2003, A&A, 412, 105

Montero-Camacho P., Fang X., Vasquez G., Silva M., Hirata C. M., 2019, J. Cosmol. Astropart. Phys., 2019, 031

Muñoz J. B., Kovetz E. D., Dai L., Kamionkowski M., 2016, Phys. Rev. Lett., 117, 091301

Nakamura T. T., Deguchi S., 1999, Prog. Theor. Phys. Suppl., 133, 137

Nakamura T., Sasaki M., Tanaka T., Thorne K. S., 1997, ApJ, 487, L139

Narayan R., 1992, Phil. Trans. R. Soc. A, 341, 151

Niikura H. et al., 2019, Nat. Astron., 3, 524

Okuta R., Unno Y., Nishino D., Hido S., Loomis C., 2017, in Proceedings of Workshop on Machine Learning Systems (LearningSys) in The Thirty-first Annual Conference on Neural Information Processing Systems (NIPS). Available at: http://learningsys.org/nips17/

Pallottini A., Ferrara A., Evoli C., 2013, MNRAS, 434, 3293

Petroff E., Hessels J. W. T., Lorimer D. R., 2019, A&AR, 27, 4

Popov S. B., Postnov K. A., Pshirkov M. S., 2018, Phys.-Usp., 61, 965

Poulter H., Ali-Haimoud Y., Hamann J., White M., Williams A. G., 2019, preprint (arXiv:1907.06485)

Press W. H., Flannery B. P., Teukolsky S. A., Vetterlin W. T., 1988, Numerical Recipes in C. Cambridge Univ. Press, Cambridge

Raidal M., Vaskonen V., Veermäe H., 2017, J. Cosmol. Astropart. Phys., 2017, 037

Raidal M., Spethmann C., Vaskonen V., Veermäe H., 2019, J. Cosmol. Astropart. Phys., 2019, 018

Ravi V. et al., 2019, Nature, 572, 352

Rickett B. J., 1977, ARA&A, 15, 479

Rickett B. J., 1990, ARA&A, 28, 561

Saito R., Yokoyama J., 2009, Phys. Rev. Lett., 102, 161101 [Erratum: Phys. Rev. Lett. 107, 069901 (2011)]

Santosa F., Symes W. W., 1986, SIAM J. Sci. Stat. Comput., 7, 1307

Sasaki M., Suyama T., Tanaka T., Yokoyama S., 2018, Class. Quantum Gravity, 35, 063001

Scalo J., Elmegreen B. G., 2004, ARA&A, 42, 275

Schutz K., Liu A., 2017, Phys. Rev. D, 95, 023002

Seto N., Cooray A., 2007, ApJ, 659, L33

Shukurov A., 2011, Introduction to Interstellar Turbulence.

Siegel E. R., Hertzberg M. P., Fry J. N., 2007, MNRAS, 382, 879

Smyth N., Profumo S., English S., Jeltema T., McKinnon K., Guhathakurta P., 2020, Phys. Rev. D, 101, 63005

Stanek K. Z., Paczynski B., Goodman J., 1993, ApJ, 413, L7

Tendulkar S. P. et al., 2017, ApJ, 834, L7

Tibshirani R., 1996, J. R. Stat. Soc. B, 58, 267

Tinyakov P., Tkachev I., Zioutas K., 2016, J. Cosmol. Astropart. Phys., 2016, 035

Tisserand P. et al., 2007, A&A, 469, 387

Ulmer A., Goodman J., 1995, ApJ, 442, 67

Vaquero A., Redondo J., Stadler J., 2019, J. Cosmol. Astropart. Phys., 04, 012

Vaskonen V., Veermae H., 2020, Phys. Rev. D, 101, 043015

Woan G., 2011, Ecole de Goutelas, 30, 147

Wyrzykowski L. et al., 2011, MNRAS, 416, 2949

Xu S., Zhang B., 2016, ApJ, 832, 199

Zhao H.-S., Taylor J., Silk J., Hooper D., 2005, preprint (arXiv:astro-ph/0502049)

Zheng Z., Ofek E. O., Kulkarni S. R., Neill J. D., Juric M., 2014, ApJ, 797, 71

Zhu W., Feng L.-L., Zhang F., 2018, ApJ, 865, 147

Zurek K. M., Hogan C. J., Quinn T. R., 2007, Phys. Rev. D, 75, 043511

This paper has been typeset from a TeX/LaTeX file prepared by the author.